Variations in oceanic plate bending along the Mariana trench

Fan Zhang,[a,b,c] Jian Lin,[c,d *] and Wenhuan Zhan[a]

[a] *Key Laboratory of Marginal Sea Geology, South China Sea Institute of Oceanology, Chinese Academy of Sciences, Guangzhou 510301, China.*

[b] *University of Chinese Academy of Sciences, Beijing 100041, China.*

[c] *Department of Geology and Geophysics, Woods Hole Oceanographic Institution, Woods Hole, MA 02543, USA.*

[d] *College of Ocean and Earth Science, Tongji University, Shanghai 200092, China.*

Abstract

We quantify along-trench variations in plate flexural bending along the Mariana trench in the western Pacific Ocean. A 3-D interpreted flexural deformation surface of the subducting Pacific Plate was obtained by removing from the observed bathymetry the effects of sediment loading, isostatically-compensated topography based on gravity modeling, age-related lithospheric thermal subsidence, and residual short-wavelength features. We analyzed flexural bending of 75 across-trench profile sections and calculated five best-fitting tectonic and plate parameters that control the flexural bending. Results of analysis revealed significant along-trench variations: the trench relief varies from 0.9 to 5.7 km, trench-axis vertical loading ($-V_0$) from -0.73×10^{12} to 3.17×10^{12} N/m, and axial bending moment ($-M_0$) from 0.1×10^{17} to 2.7×10^{17} N. The effective elastic plate thickness seaward of the outer-rise region (T_e^M) ranges from 45 to 52 km, while that trench-ward of the outer-rise (T_e^m) ranges from 19 to 40 km. This corresponds to a reduction in T_e of 21-61%. The transition from T_e^M to T_e^m occurs at a breaking distance of 60-125 km from the trench axis, which is near the outer-rise and corresponds to the onset of observed pervasive normal faults. The Challenger Deep area is associated with the greatest trench relief and axial

vertical loading, while areas with seamounts at the trench axis are often associated with more subtle trench relief, smaller axial vertical loading, and greater topographic bulge at the outer-rise.

Keywords: Mariana trench; Axial vertical force; Axial bending moment; Effective elastic thickness

*Corresponding Author.

E-mail address: jlin@whoi.edu (J. Lin).

1. Introduction

The greatest flexural bending of Earth's oceanic lithosphere occurs at subduction zones. During subduction, the downgoing plate flexes in response to various types of tectonic forces, e.g., trench-axis vertical loading, axial bending moment, distributed sediment loading, and horizontal buckling. The flexural bending produces distinct seafloor sloping towards the trench axis, as well as gentle upward seafloor bulging near the outer-rise region seaward of the trench (e.g., Hanks, 1971; Bodine and Watts, 1979; Harris and Chapman, 1994; Bry and White, 2007). Furthermore, as flexural deformation becomes significant, bending stresses could exceed the rock yield strength within the most deformed portions of the lithosphere (e.g., McNutt and Menard, 1982; Ranalli, 1994), causing pervasive faulting and tensional earthquakes in the upper plate (Christensen and Ruff, 1983; Masson, 1991; Ranero et al., 2005; Naliboff et al., 2013), local plastic yielding (Turcotte et al., 1978; Bodine and Watts, 1979; McNutts, 1984; McAdoo et al., 1985), and a noticeable reduction in the effective elastic thickness of the plate, especially near the outer-rise region (Judge and McNutt, 1991; Levitt and Sandwell, 1995; Watts, 2001; Billen and Gurnis, 2005; Contreras-Reyes and Osses, 2010). Thus the observed spatial variations

in flexural bending of a specific subducting plate could provide important constraints on trench tectonic loading and lithospheric strength (e.g., Mueller and Phillips, 1995; Capitanio et al., 2009; Capitanio and Morra, 2012).

In this study, we investigated variations in flexural bending along the Mariana trench of the western Pacific Ocean (Fig. 1). We chose the Mariana trench as a study area for several reasons: (1) it exhibits significant along-trench changes in trench depth, slope, and outer-rise bulge (Fig. 2); (2) it contains the greatest trench depth of the world, the Challenger Deep, with trench depth of about 10.9 km and trench relief of 5.7 km (Fig. 2); (3) high-resolution multi-beam bathymetric data are available for a significant portion of the trench axis and the outer-rise region, aiding the identification of detailed features; and (4) the 20-Ma difference in the crustal age of the subducting plate is relatively small comparing to the overall age of 140-160 Ma, thus facilitating analysis of factors unrelated to plate age.

A major challenge in flexural bending analysis is the identification of the "deformed shape" of a subducting plate from the complex seafloor topography that contains many other features unrelated to flexural bending, such as seamounts and volcanic ridges. Previous studies attempted to bypass this problem by choosing sparse topographic and free-air gravity profiles away from seamounts and ridges or designating these features as part of data uncertainties (e.g., Bodine and Watts, 1979; Judge and McNutt, 1991; Levitt and Sandwell, 1995; Billen and Gurnis, 2005; Bry and White, 2007; Contreras-Reyes and Osses, 2010). However, in regions that contain abundant seamounts and ridges, such as near the Mariana trench (Fig. 2), these traditional approaches are inadequate for investigating the spatial variations in plate bending. In this paper, we present a new approach in identifying the deformed shape of a bending plate. Instead of using seafloor bathymetry directly, we conduct the analysis in two steps: First, we calculated "non-isostatic"

topography by removing from the observed bathymetry the effects of sediment loading, isostatically-compensated topography based on gravity modeling, and age-related lithospheric thermal subsidence. By removing these non-flexural effects, the resultant "non-isostatic" topography proves to be a much-improved approximation to the deformed shape of a bending plate. Second, we further removed short-wavelength features from the "non-isostatic" topography to obtain an interpreted 3-D surface of plate flexural bending.

We adopted a simplified model of a lithospheric plate of varying effective elastic thickness overlying an inviscid asthenosphere and analyzed flexural bending along 75 across-trench sections, each consists of ten profiles spanning over an along-trench distance of about 0.2°. Our analysis illustrated that these observed plate bending profiles could be explained by flexural deformation models assuming various forms of spatial variations in plate thickness. However, the vast majority of the observed plate bending profiles could be adequately reproduced by a simplified model, in which the deforming plate has only two characteristic values of effective elastic thickness, seaward (T_e^M) and trench-ward (T_e^m), respectively, of a breaking point near the outer-rise region. For each section, we then calculated five best-fitting parameters including axial vertical force ($-V_0$), axial bending moment ($-M_0$), maximum effective elastic thickness (T_e^M), minimum elastic thickness (T_e^m), and the breaking point distance (x_r) between sections of the maximum and minimum elastic thickness. Modeling results revealed significant changes in tectonic loading and plate deformation along the Mariana trench.

2. Identification of Plate Deformation Caused by Flexural Bending

To better identify plate flexural bending near the trench axis, we first subtracted from the observed seafloor bathymetry the following predictable components that are not directly related

to trench-axis plate bending: (1) sediment loading; (2) isostatically-compensated topography, including features such as seamounts and volcanic ridges with crustal roots, calculated through gravity analysis; and (3) age-related lithospheric thermal subsidence (Muller et al., 2008) assuming 1-D vertical cooling of the lithosphere. The resultant "non-isostatically-compensated topography" should reflect primarily the topographic features that are dynamically supported by stresses in the lithospheric plate, including trench-related plate bending, as well as uncertainties in the above estimation of various loading features.

(1) *Seafloor Bathymetry*. We constructed a bathymetric database with grid spacing of 0.25' (Fig. 2), which combines two primary data sources: (1) high-resolution multi-beam bathymetric data from the database of the National Geophysical Data Center (NGDC, Lim et al., 2013); and (2) the GEBCO08 data with grid spacing of 0.5' (http://www.gebco.net). Our study area covers a total along-trench distance of about 2,500 km, where multi-beam data are available for the distance of 100-2,000 km (Fig. 9). The trench depth (blue curve in Fig. 6a) is about 5-7 km near the Caroline Ridge (Region 1, at distance of 0-250 km, Fig. 2). At the Challenger Deep (at distance of about 400 km), the trench reaches a maximum depth of about 10.9 km. Another area of relatively deep trench is located at distance of about 650 km. The trench depth shows long-wavelength decrease northward. Prominent seamounts are located on the trench axis at distance of 1,350, 1,600, 1,800, and 2,300 km, respectively, reducing the local trench depth to only 5-6 km (Figs. 2 and 6a).

The seafloor bathymetry also varies significantly seaward of the trench axis. The Caroline Ridge (Region 1, Fig. 2) is located near and off the trench axis at distance of about 0-250 km, while the Caroline Islands Chain (Region 2) intersects the trench axis at distance of about 600-700 km. A prominent trench-parallel belt of seamounts (Region 3), with trench-perpendicular

width of about 250 km, appears at distance of 800-1,350 km. Another prominent group of seamounts, with relatively wide seamount bases and shallow apexes (Region 4), intersects the trench axis at distance of 1,600-2,000 km. At a section of oblique subduction (at distance of 2,000-2,400 km), seamounts are absent seaward of the trench axis within 250 km. Starting at distance of 2,400 km and northward, another prominent ridge (Region 5) approaches the trench axis.

(2) *Sediment Loading*. We extracted sediment thickness data from the NGDC sediment database (Divins, 2003) with grid spacing of 5' (Fig. 3a). Thick sediments appear in four regions: the southwest corner of the Caroline Ridge region (up to 0.6 km of sediment thickness); the eastern part of the study area at latitude 6°-15°N (up to 0.5 km); an off-axis region at latitude 17°-23°N (up to 0.6 km); and a narrow belt along the trench axis at latitude 12.5°-22°N (up to 0.25 km). For the rest of the study region, the interpolated sediment thickness is less than 0.1 km. However, the interpolated sediment grids likely have under-sampled the true local sediment thickness.

(3) *Isostatically-Compensated Topography*. For topographic features that are locally compensated, e.g., seamounts and ridges with crustal roots, we calculated the isostatic topography based on Airy-Heiskanen model. The isostatic topography is calculated as $T_{iso} = (H_c - \overline{H_c}) \times (\rho_m - \rho_c) / (\rho_m - \rho_w)$, where H_c is the gravity-derived crustal thickness, $\overline{H_c}$ is a reference crustal thickness, and ρ_w, ρ_c, and ρ_m are densities of water, crust, and mantle, respectively (Table 1). We used gravity-derived crustal thickness (Fig. 3c) calculated from gravity inversion using methods similar to Parker (1973), Kuo and Forsyth (1988), and Wang et al. (2011) and calibrated using available seismic data (see Appendix C in Supplementary Materials).

Several regions are associated with relatively thick crust (Fig. 3c) and thus high values of calculated isostatic topography: a broad region close to the Caroline Ridge and Caroline Islands Chain at 6°-12°N (Regions 1 and 2, up to 27 km of crustal thickness and 5.5 km of isostatic topography); a trench-parallel belt at 12°-16.5°N (Region 3, up to 18 km crust and 3.2 km of isostatic topography); two E-W trending seamount groups at 17°-21.5°N (Region 4, up to 20 km crust and 3.7 km of isostatic topography); and an NW-SE trending group of ridges and seamounts at 25°-27.5°N (Region 5, also up to 20 km crust and 3.7 km of isostatic topography). For the rest of the study region, the calculated crustal thickness is about 3-6 km, corresponding to isostatic topography of -0.8 to 0 km.

(4) *Non-Isostatically-Compensated Topography*. We calculated non-isostatic topography ($T_{n\text{-}iso}$) by removing from the observed bathymetry (Fig. 2) the effects of sediment loading (Fig. 3a), thermal subsidence, and isostatically-compensated topography (T_{iso}). On the map of non-isostatic topography (Fig. 3d), the most prominent feature is low topography along the Mariana trench with maximum depth near the Challenger Deep. The Caroline Ridge and Caroline Islands Chain are associated with much more subdued features in the map of non-isostatic topography (Fig. 3d) than in the map of observed bathymetry (Fig. 2). Similarly, some of the seamounts are more subduced in the non-isostatic topography than in the observed bathymetry. We suggest that the remaining short-wavelength non-isostatic topography of the ridges and seamounts are either supported by stresses in the lithospheric plate or due to inherent uncertainties in the estimation of crustal thickness using gravity analysis. Along the trench axis, the non-isostatic topography shows great long-wavelength variations with minimum values at along-trench distances of about 400 km (Challenger Deep) and 650 km (black curve in Fig. 6b). The long-wavelength along-trench variations are greatly reduced on trench-parallel profiles taken at across-trench distances

of 100 km (the outer-rise region, red curve in Fig. 6b) and 550 km (far field, blue curve in Fig. 6b). This suggests that the great along-trench axis variations in the non-isostatic topography (black curve in Fig. 6b) could reflect the significant along-trench variability in flexural bending of the subducting plate.

(5) *Flexural Bending of the Subducting Plate.* We extracted a total of 750 across-trench profiles, each of 600-km long, spanning at an interval of 0.02° (about 3.3 km) along the Mariana trench. Every ten profiles were stacked together to form a section (e.g., Figs. 4b-d), resulting in a total of 75 sections (Fig. 5; Figs. S1-8 of Appendix A in Supplementary Materials). For each section, we determined a flexural bending model (red dashed curves, Figs. 4 and 5; Figs. S1-8 in Supplementary Materials) that best captures the long-wavelength characteristics of the non-isostatic topography profile both across the trench strike (blue curves, Figs. 4 and 5; Figs. S1-8 in Supplementary Materials) and along the trench strike (Fig. 6b). On several across-trench sections (e.g., Sections 1-5, 56-58, 72-75), seamounts have covered up the trench axis or obscured a significant portion of the far-field reference seafloor depth (Supplementary Table 1). When estimating the overall shape of flexural bending, we ignored short-wavelength features of the seamounts and their periphery depression in the non-isostatic topography (Figs. 4 and 5; Figs. S1-8 in Supplementary Materials). The 75 sections were then interpolated to create a map of flexural bending (Fig. 3e). The greatest flexural bending occurs at along-trench distance of 350-650 km, including the Challenger Deep. The different between the non-isostatic topography (Fig. 3d) and the flexural bending model (Fig. 3e) is showing as a map of residuals (Fig. 3f), which appears to contain primarily local features such as seamounts and surrounding depression.

3. Modeling of Plate Flexural Bending

In thin-plate approximation, the vertical deflection of a plate is governed by the balance among various forces (Turcotte and Schubert, 2002):

$$-\frac{d^2M}{dx^2}+\frac{d}{dx}(F\frac{dw}{dx})+(\rho_m-\rho_w)gw=(\rho_s-\rho_w)gh_s(x), \quad (1)$$

where M is bending moment, F is horizontal buckling force, $(\rho_m-\rho_w)gw$ represents hydrostatic restoring force, $(\rho_s-\rho_w)gh_s(x)$ is vertical sediment loading, and ρ_s and h_s are the sediment density and thickness, respectively.

The bending moment is proportional to the vertical deflection by $M=-D\frac{d^2w}{dx^2}$, where flexural rigidity $D=\frac{ET_e^3}{12(1-\nu^2)}$, E is Young's modulus, ν is Poisson's ratio, and T_e is effective elastic plate thickness. The vertical force is related to both the bending moment and horizontal force by $V=\frac{dM}{dx}-F\frac{dw}{dx}$. As a first-order approximation, we ignored the horizontal buckling force similar to the analyses of Caldwell et al. (1976), Molnar and Atwater (1978), and Contreras-Reyes and Osses (2010). Constant parameters assumed in the analysis are described in Table 1. Boundary conditions of the vertical deflection include the following: w = 0 and $\frac{dw}{dx}=0$ at x = $+\infty$, while $D\frac{d^2w}{dx^2}=-M_0$ and $\frac{dM}{dx}=-V_0$ at x = 0.

We used a simplified model of an elastic plate of two effective elastic thickness values. We assumed that the effective elastic thickness changes from T_e^M (seaward of the outer-rise) to T_e^m (near the trench axis), in order to simultaneously replicate the observed steep slope trench-ward of the outer-rise as well as the relatively long flexural wavelength seaward of the outer-rise region (Turcotte et al. 1978; Judge and McNutt 1991). The transition occurs at a breaking

distance x_r near the outer-rise (Fig. 4a). The reduced effective elastic thickness is assumed to reflect the onset of pervasive normal faulting within the upper plate near the outer-rise (Fig. 4a).

(1) *Calculation of Trench-Axis Vertical Force*. We found that the vertical force at the trench axis is proportional to the total area of the vertical deflection integrated over the entire across-trench profile. For the case of a constant plate thickness, the vertical deflection (Turcotte and Schubert, 2002) is given by $w(x)=\frac{\alpha^2 e^{-x/\alpha}}{2D}\left[-M_0\sin(\frac{x}{\alpha})+(V_0\alpha+M_0)\cos(\frac{x}{\alpha})\right]$, where the flexural wavelength α is defined by $\alpha=\left[\frac{4D}{(\rho_m-\rho_w)g}\right]^{1/4}$. Direct integration of the above equation yields

$$-V_0=(\rho_m-\rho_w)g\int_0^{+\infty}w(x)dx\,. \qquad (2)$$

We conducted a series of tests for deflection of plates with variable thickness and found that the above Eqn. 2 still holds for cases when the effective plate thickness varies horizontally. Thus by integrating the interpreted vertical deflection of a given profile (Fig. 5), we can readily calculate the trench-axis vertical force (Fig. 6c and Supplementary Table 1).

(2) *Inversion of Axial Bending Moment and Plate Thickness Variation*. We next inverted for four best-fitting parameters, $-M_0$, T_e^M, T_e^m, and x_r, for each section. Using the finite-difference method of Contreras-Reyes and Osses (2010), we discretized each profile section into a series of nodes with a uniform spacing of 3 km (see Appendix B in Supplementary Materials). Sediment loading was prescribed at each node point. For each section, we then inverted for a set of best-fitting parameters that minimize the root mean square (RMS) misfit between the non-isostatic topography ($T_{n\text{-}iso}$, blue curves in Figs. 4 and 5; Figs. S1-8 in Supplementary Materials) for areas

224 away from seamounts and the flexural bending model (red dashed curves in Figs. 4 and 5; Figs.
225 S1-8 in Supplementary Materials).
226
227 **4. Results**
228 Results of analysis revealed that both the trench-axis loading and plate thickness vary
229 significantly along the Mariana trench.
230 **4.1 Along-Trench Variations in Trench Relief and Axial Loading**
231 The trench relief, which was calculated from subtracting the trench-axis depth from a far-field
232 reference depth, varies from 0.9 to 5.7 km along the Mariana trench (black curve in Fig. 6a and
233 Supplementary Table 1). Within the first 230 km from the southwestern end of the trench, the
234 trench relief ranges from 1.7 to 3.4 km. The greatest trench relief of 5.7 km is at the Challenger
235 Deep. Another area of large trench relief of about 5.2 km is located east of the Challenger Deep
236 at along-trench distance of about 650-670 km (Fig. 6a). In between the above two deep locations,
237 the Caroline Islands Chain (Region 2, Fig. 2) has trench relief of about 4.0 km (Fig. 6a). From
238 distance of 850 to 1,250 km, the trench relief gradually decreases from 3.9 to 1.8 km. From
239 1,250 to 2,250 km, the trench relief ranges from 1.4 to 3.0 km with prominent trench-axis highs
240 located at 1,250-1,300 km, 1,600-1,650 km, 1,950-2,050 km, respectively. The section of the
241 trench at distance of 1,950-2,300 km, which is associated with relatively oblique convergence
242 angles, has trench relief of 1.4 to 2.2 km.
243 The calculated axial vertical force (Fig. 6c) is in general proportional to the trench relief (Fig.
244 6a). The two areas of great trench relief, at the Challenger Deep and its eastern section, were
245 calculated to be subjected to large axial vertical loading of 3.17×10^{12} N/m and 2.1×10^{12} N/m,
246 respectively (Supplementary Table1). Along the Mariana trench, several areas are associated

with upward, instead of downward, vertical force of small magnitude (red arrows in Fig. 6c and black arrows in Fig. 3b; Supplementary Table 1); these sections account for more than 20% length of the Mariana trench. The total trench-axis vertical force integrated over the 2,500-km-long study area is about 1.66×10^{18} N; sections with trench relief greater than 3.0 km contribute to more than 80% of the total vertical force. The axial vertical force averaged over the trench length is about 0.67×10^{12} N/m.

The calculated trench-axis bending moment (Fig. 6d; Supplementary Table 1) also appears to be correlated with trench relief (Figs. 6a). The axial bending moment is the smallest ($-M_0 = 0.1 \times 10^{17}$ N) near the Challenger Deep (Fig. 6d). In contrast, the bending moment is in general greater for sections of relatively small trench relief. The calculated bulge height at the outer-rise (w_b) ranges from 70 to 650 m (Supplementary Table 1). The bulge height is the smallest at the Challenger Deep area (w_b = 70 m), while large bulge height (w_b > 500 m) is associated with sections of relatively large axial bending moment ($M_0 > 2.4 \times 10^{17}$ N) at distance of 920-1,000, 1,070-1,090, and 1,390-1,440 km (Supplementary Table 1). The across-trench distance of the bulge height (x_b, blue curve in Fig. 6g) varies in the range of 69-180 km from the trench axis.

4.2 Along-Trench Variations in Effective Elastic Thickness

To replicate the far-field long-wavelength flexural bending, the effective elastic thickness of the plate seaward of the outer-rise (T_e^M) is calculated to range from 45 to 52 km (blue curve in Fig. 6e; Supplementary Table 1). However, to replicate the observed steep seafloor slope towards the trench axis, the effective elastic thickness trench-ward of the outer-rise (T_e^m) is only 19 to 40 km (black curve in Fig. 6e). The transition from T_e^M to T_e^m occurs at a breaking distance x_r = 60-125 km from the trench axis (black curve in Fig. 6g). The resultant reduction in the effective elastic thickness, i.e., 1 - (T_e^m/T_e^M), is in the range of 21-61% (Fig. 6f). The greatest reduction in

T_e is about 61%, occurring near the Challenger Deep area, where the plate bends significantly within a narrow distance of x_r = 75-85 km. Reduction in T_e of greater than 50% also occurs at four other areas at distance of 0-50, 1,180-1,230, 1,490-1,510, 1,760-1,860 km, respectively, where the calculated breaking distance is relatively small (x_r < 90 km, Fig. 6g; Supplementary Table 1). In contrast, areas with smaller reduction in elastic thickness (< 30 %), e.g., at distance of 160-250, 1,320-1,350, 1,460-1,490, 1,560-1,610, and 1,980-2,140 km, are associated with large breaking distance (x_r > 100 km, Fig. 6g; Supplementary Table 1) or smaller trench relief (< 2 km) (blue dots in Fig. 7b). Our results revealed that the reduction in T_e along the Mariana trench does not exceed 61%, implying that an elastic core remains in the subducting plate despite pervasive normal faulting caused by flexural bending near the trench axis (Fig. 4a).

For a plate of constant elastic thickness, the trench relief can be calculated as $w_0 = \frac{\alpha^2 (V_0 \alpha + M_0)}{2D}$, where flexural wavelength α and flexural rigidity D are a function of T_e. We compared the observed trench relief with the predicted values for the end-member cases of $T_e = T_e^m$ and T_e^M, respectively (Fig. 7a). The w_0 calculated assuming $T_e = T_e^m$ is only 8 % greater than the observed values with a regression coefficient of 0.99. This implies that the observed trench relief is controlled primarily by T_e^m, and not by T_e^M .

5. Discussion

5.1 Uncertainties in Data and Analysis

Several aspects of the above analysis might be associated with uncertainties. (1) The northern most 500-km of the trench-axis (~21°-25°N) lacks high-resolution multi-beam bathymetric data (Fig. 9). While lacking multi-beam bathymetry is not likely to affect significantly our inverted flexural bending parameters, it would prevent the identification of the onset location of normal

faults (Fig. 9). (2) The data coverage of sediment thickness might be highly non-uniform and sparse for much of the study region. However, our example test for Section 49, which has a maximum sediment thickness of 0.4 km, showed that the inverted flexural parameters change little with versus without considering sediment loading. Thus we infer that the lack of high-resolution data of sediment thickness might not change the overall pattern of the calculated flexural parameters. (3) There are inherent uncertainties associated with gravity-derived crustal thickness (e.g., Wang et al., 2011), leading to uncertainties in the calculated isostatic and non-isostatic topography. These uncertainties, however, are difficult to quantify without independent seismic constraints.

The subducting Pacific plate is concave along the Mariana trench. Bonnardot et al. (2008) numerically modeled the effects of trench curvature on the deformation of a subducting plate for different curvature radius values. We interpolated their modeling results for the estimated curvature values of the Mariana trench. The trench curvature appears to have greater effects on the modeling of axial vertical loading than on other parameters.

5.2 Unique Characteristics of the "Seamount" Sections

While the trench relief is most sensitive to the axial vertical force, the predicted topographic bulge height at the outer-rise is much more sensitive to the axial bending moment. We separated the 75 sections of the Mariana trench into four groups according to the average value of the calculated axial vertical force (Fig. 8a). The averaged value of the calculated trench relief is greater for sections of larger vertical force. In contrast, the averaged value of the bulge height at the outer-rise is greater for sections of larger axial bending moment (Fig. 8b).

Several areas of the Mariana trench are associated with small amplitudes of upward axial vertical force (red arrows in Fig. 6c). The averaged across-trench profiles of these "seamount"

316 sections (striped belt in Fig. 8c) are of relatively small vertical force. We further noted that these
317 “seamount” sections are associated with relative large topographic bulge at the outer-rise
318 (Supplementary Table 1). The averaged height of the topographic bulge for these “seamount”
319 sections is 388 m, which is much greater than the averaged value of 288 m for the remaining
320 “non-seamount” sections. Correspondingly, the calculated axial bending moment for individual
321 “seamount” sections (Fig. 6d), as well as the averaged bending moment for all “seamount”
322 sections (Fig. 8d), are greater than that of “non-seamount” sections. While the observed higher
323 topographic bulge at the outer-rise could be caused by greater axial bending moment for the
324 “seamount” sections, they might also be caused by significant horizontal buckling force in the
325 plate, due to the resistance of the seamounts to subduction, which was not modeled in the present
326 analysis.

327 **5.3 Causes of Reduction in Elastic Plate Thickness**

328 Results of analysis indicated a reduction in the effective plate thickness of 21-61% near the
329 outer-rise region along the Mariana trench (Fig. 6f). Thus lateral changes in the plate property
330 are likely to be significant, while the specific values of the plate thickness reduction depend on
331 our specific model assumptions. Similar results were obtained from analysis of the central
332 Mariana trench (Oakley et al., 2008).

333 We hypothesize that the calculated reduction in the effective elastic thickness reflects the
334 effects of pervasive normal faulting in a bending plate (Fig. 4a). Under the trench-axis loading,
335 the upper half of the bending plate would be in extension while the lower plate would be under
336 compression. Computational geodynamic models showed that the loss of rock cohesion and
337 strain weakening caused by slip on normal faults could significantly reduce the effective elastic
338 strength of a lithospheric plate (Rupke et al, 2004; Faccenda et al., 2009).

339 The development of normal faults is likely to be distributed over a broad region, and thus the
340 reduced elastic thickness T_e^m and the breaking distance x_r are over simplifications. Nevertheless,
341 the location of the calculated x_r in general appears to be consistent with the observed outer
342 boundary of a zone of pervasive normal faults at sections with multi-beam bathymetry coverage
343 (Fig. 9). The Challenger Deep area of the Mariana trench is associated with a relatively large
344 reduction in the effective elastic thickness, which might reflect relatively extensive normal
345 faulting in response to the large axial vertical force (Fig. 9b).
346
347 **6. Conclusions**
348 1. Results of analysis revealed significant variations in trench-axis loading and plate
349 mechanical property along the Mariana trench. The trench relief varies from 0.9 to 5.7 km; the
350 trench-axis vertical force varies from -0.73×10^{12} to 3.17×10^{12} N/m; and the axial bending
351 moment varies from 0.1×10^{17} to 2.7×10^{17} N.
352 2. Modeling of long-wavelength flexural bending seaward of the outer-rise region indicates
353 that the effective elastic plate thickness of the incoming plate (T_e^M) to be in the range of 45-52
354 km. Trench-ward of the outer-rise, the observed steep seafloor slope indicates thinner effective
355 elastic thickness (T_e^m) of 19-40 km; the corresponding reduction in T_e is 21-61%. The transition
356 from T_e^M to T_e^m occurs at a breaking distance of 60-125 km from the trench axis, corresponding
357 to the onset of the observed zones of pervasive normal faulting.
358 3. The Challenger Deep area in the southwestern Mariana trench is associated with the
359 greatest trench relief, axial vertical loading, and reduction in T_e. Several areas with seamounts at
360 the trench axis are associated with shallower trench relief, smaller axial vertical force, and higher
361 topographic bulge at the outer-rise.

Acknowledgements. We are grateful to Dr. Eduardo Contreas-Reyes for providing finite-difference codes for calculating flexural bending of a thin plate with variable effective elastic thickness. We benefited from technical assistance from Jian Zhu and Zhiyuan Zhou, constructive comments and suggestions by two reviewers, as well as discussion with Min Ding, Minqiang Tang, Mark Behn, Jeff McGuire, Nathan Miller, Dan Lizarralde, Yajing Liu, Longtao Sun, Yen Joe Tan, and the WHOI Marine Tectonics Group. This work was supported by US NSF Grant OCE-1141985 and Deerbrook Foundation (J.L.), NSF-China Grant 41376063 and Joint NSF-China/Guangdong Natural Science Fund Committee U0933006 (W.Z.), and the Chinese Scholarship Council (F.Z.).

References

Billen, M.I., Gurnis, M., 2005. Constraints on subducting plate strength within the Kermadec trench, J. Geophys. Res., 110, doi:10.1029/2004JB003308.

Bird, P., 2003. An updated digital model of plate boundaries, Geochem., Geophys., Geosyst., 4, doi:10.1029/2001GC000252.

Bodine, J.H., Watts, A.B., 1979. On the lithospheric flexure seaward of the Bonin and Mariana Trenches, Earth Planet. Sci. Lett. 43, 132–148.

Bonnardot, M.A., Hassani, R., Tric, E., Ruellan, E., Regnier, M., 2008. Effect of margin curvature on plate deformation in a 3-D numerical model of subducton zones, Geophys. J. Int. 173, 1084-1094.

Bry, M., White, N., 2007. Reappraising elastic thickness variation at oceanic trenches, J. Geophys. Res. 112, doi:10.1029/2005JB004190.

385 Caldwell, J.G., Haxby, W.F., Karig, D.E., Turcotte, D.L., 1976. On the applicability of a
386 universal elastic trench profile, Earth Planet. Sci. Lett. 31, 239–246.
387 Capitanio, F.A., Morra, G., 2012. The bending mechanics on a dynamic subduction system:
388 Constraints from numerical modelling and global compilation analysis, Tectonophys., 522-
389 523, 224–234.
390 Capitanio, F.A., Morra, G., Goes, S., 2009. Dynamics of plate bending at the trench and slab-
391 plate coupling, Geochem., Geophys., Geosyst., 10,
392 doi:10.1029/2008GC002348.
393 Christensen, D.H., Ruff, L.J., 1983. Outer-rise earthquakes and seismic coupling, Geophys. Res.
394 Lett. 10, 697-700.
395 Contreras-Reyes, E., Osses, A., 2010. Lithospheric flexure modelling seaward of the
396 Chiletrench: Implications for oceanic plate weakening in the trench outer rise region,
397 Geophys. J. Int. 182, 97-112.
398 Divins, D., 2003. Total sediment thickness of the world's oceans and marinal seas. NOAA
399 National Geophysical Data Center, Boulder, CO.
400 http://www.ngdc.noaa.gov/mgg/sedthick/sedthick.html
401 Faccenda, M., Gerya, T.V., Burlini, L., 2009. Deep slab hydration induced by bending-related
402 variations in tectonic pressure, Nat. Geosci. 2, 790-793.
403 Hanks, T.C., 1971. The Kuril trench-Hokkaido Rise system: Large shallow earthquakes and
404 simple models of deformation, Geophys. J. R. Astr. Soc., 23, 173.
405 Harris, R., Chapman, D., 1994. A comparison of mechanical thickness estimates from trough and
406 seamount loading in the southeastern Gulf of Alaska, J. Geophys. Res, 95, 9297-9317.
407 Judge, A.V., McNutt, M.K., 1991. The relationship between plate curvature and elastic plate

thickness: A study of the Peru-Chile Trench, J. Geophys. Res. 96, 16625–16639.

Kuo, B-Y., Forsyth, D.W., 1988. Gravity anomalies of the ridge-transform system in the South Atlantic between 31° and 34.5°S: Upwelling centers and variations in crustal thickness, Marine Geophys. Res. 10, 205-232.

Levitt, D.A., Sandwell, D.T., 1995. Lithospheric bending at subduction zones based on depth soundings and satellite gravity, J. Geophys. Res. 100, 379–400.

Lim, E., Sutherland, M.G., Friday, D.Z., Eakins, B.W., and McLean, S.J., 2013. Bathymetric Digital Elevation Model of the Mariana Trench, NOAA National Geophysical Data Center, U.S. Dept. of Commerce, Boulder, CO, 4 pp.

Masson, D.G., 1991. Fault patterns at outer trench walls, Mar. Geophys. Res., 13, 209-225.

McAdoo, D.C., Martin, C.F., Poulose, S., 1985. Seasat observations of flexure: Evidence for a strong lithosphere, Tectonophys., 116, 209–222.

McNutt, M.K., 1984. Lithospheric flexure and thermal anomalies, J. Geophys. Res., 89, 11,180–11,194.

McNutt, M.K., Menard, H.W., 1982. Constraints on yield strength in the oceanic lithosphere derived from observations of flexure, Geophys. J. R. astr. Soc., 71, 363-394.

Molnar, P., Atwater, T., 1978. Interarc spreading and cordilleran tectonics as alternates related the age of subducted oceanic lithosphere. Earth planet. Sci. Lett. 41, 330–340.

Müller, R.D., Sdrolias, M., Gaina, C., Roest, W.R., 2008. Age, spreading rates, and spreading asymmetry of the world's ocean crust, Geochem., Geophys., Geosyst., 9, doi:10.1029/2007GC001743.

Mueller, S., Phillips, R.J., 1995. On the reliability of lithospheric constraints derived from models of outer-rise flexure, Geophys. J. Int., 123, 887-902.

Naliboff, J.B., Billen, M.I., Gerya. T., Saunders. J., 2013. Dynamics of outer-rise faulting in oceanic-continental subduction systems, Geochem., Geophys., Geosyst., 14, doi:10.1002/ggge.20155.

Oakley, A.J., Taylor, B., Moore, G.F., 2008. Pacific plate subduction beneath the central Mariana and Izu-Bonin fore-arcs: New insights from an old margin, Geochem., Geophys., Geosyst., 9, doi:10.1029/2007GC001820.

Parker, R.L., 1973. The rapid calculation of potential anomalies. Geophys. J. Roy. Astron. Soc. 31, 447-455.

Ranalli, G., 1994. Nonlinear flexure and equivalent mechanical thickness of the lithosphere, Tectonophys. 240, 107-114.

Ranero, C.R., Villaseor, A., Phipps Morgan, J., and Wdinrebe, W., 2005. Relationship between bending-faulting at trenches and intermediate-depth seismicity. Geochem., Geophys., Geosyst., 6, doi:10.1029/2005GC000997.

Rupke, L.H., Morgan, J.P., Hort, M., Connolly, J.D.L., 2004. Serpentine and the subduction zone water cycle. Earth Planet. Sci. Lett. 223, 17–34.

Turcotte, D.L., McAdoo, D.C., Caldwell, J.G., 1978. An elastic-perfectly plastic analysis of the bending of the lithosphere at a trench. Tectonophys., 47, 193-208.

Turcotte, D., Schubert, G., 2002. Geodynamics, 2nd Edition, Cambridge University Press, New York, 456 pp.

Sandwell, D.T., and Smith, W.H.F., 2009. Global marine gravity from retracked Geosat and ERS-1 altimetry: Ridge segmentation versus spreading rate. J. Geophys. Res., 114, B01411, doi:10.1029/2008JB006008.

Wang, T., Lin, J., Tucholke, B., Chen, Y.J., 2011. Crustal thickness anomalies in the North

454 Atlantic Ocean basin from gravity analysis. Geochem., Geophys., Geosyst., 12,
455 doi:10.1029/2010GC003402.
456 Watts, A.B., 2001. Isostasy and flexure of the lithosphere, Cambridge University Press, New
457 York, 458 pp.
458

459 **Figure Captions**

460 **Figure 1.** Tectonic map of the western Pacific Ocean including the Mariana trench. The Pacific
461 Plate is subducting under the Mariana and Philippines Plates (Bird, 2003). Challenger Deep is
462 the deepest part of the Mariana trench and the world. Dashed lines mark the study region of Fig.
463 2.

464

465 **Figure 2.** Seafloor bathymetry of the Mariana trench and surrounding regions. Dashed lines
466 mark the study area as shown in Fig. 3. Along-trench distance is measured from the southwestern
467 end of the Mariana trench. Circled numbers indicate tectonic provinces discussed in the text.

468

469 **Figure 3.** Maps of the study area. (a) Sediment thickness. (b) Basement depth. Black arrows
470 indicate sections experiencing small upward instead of downward vertical force (along-trench
471 locations shown in Fig. 6c). (c) Crustal thickness calculated from gravity analysis. This map is
472 used to calculate isostatic topography due to crustal thickness variations. (d) Non-isostatic
473 topography. (e) Flexural bending model interpolated from results along across-trench sections.
474 Results from profile sections of relatively poor constraints due to significant seamount effects are
475 not shown. (f) Residuals showing the difference between non-isostatic topography (panel d) and
476 flexural bending model (panel e).

477

478 **Figure 4.** (a) Schematic model of plate flexural bending. The vertical force ($-V_0$) and bending
479 moment ($-M_0$) are applied at the trench axis. Distance x_r is where the effective elastic thickness is
480 reduced from T_e^M to T_e^m. Distance x_b is the location of maximum uplift at the outer-rise. Area
481 with stripes illustrates the approximate location of expected pervasive normal faulting failure in a

zone of tectonic extension within the upper plate; the effective elastic thickness of this section of the plate is reduced to T_e^m due to mechanical weakening by normal faulting. (b), (c), and (d) correspond to sections of the greatest curvature, greatest trench relief, and shallowest section along the Mariana trench, respectively. Basement topography of every ten individual profiles was stacked to form an averaged section for modeling: grey and green curves show areas with and without multi-beam bathymetry, respectively. Blue curves are the calculated non-isostatic topography. Red dashed curves show flexural bending models that best fit non-isostatic topography away from seamounts.

Figure 5. Fourteen example sections of flexural bending at different locations along the Mariana trench. Basement topography of every ten individual profiles was stacked to form an averaged section for modeling: grey and green curves show areas with and without multi-beam bathymetry, respectively. Blue curves are the calculated non-isostatic topography. Red dashed curves show flexural bending models that best fit non-isostatic topography away from seamounts.

Figure 6. Tectonic variables and calculated parameters along the Mariana trench. In panels c-g, results from profile sections of relatively poor constraints due to significant seamount effects are not shown. (a) Blue curve is the observed trench depth. Black curve is trench relief (measured from a far-field reference seafloor depth to the trench axis). (b) Calculated non-isostatic topography on trench-parallel profiles along the trench axis (black curve), near the outer-rise region (100 km away from the trench axis, red curve), and at the far-field (550 km from the trench axis, blue curve). (c) Calculated trench-axis vertical loading ($-V_0$). Red arrows indicate sections that are subjected to small upward vertical loading. (d) Calculated axial bending

505 moment (-M_0). (e) Calculated effective elastic thickness. Blue and black curves mark the
506 maximum and minimum elastic thickness T_e^M and T_e^m, respectively. (f) Calculated reduction
507 from T_e^M to T_e^m. (g) Blue and black curves mark the across-trench distances for locations of the
508 maximum bulge height near the outer-rise region (x_b) and the transition from the maximum to
509 minimum effective elastic thickness (x_r), respectively.
510
511 **Figure 7.** (a) Correlation of the observed trench relief with the calculated trench relief (w_0) for a
512 constant plate thickness model assuming $T_e = T_e^m$ (red dots) and $T_e = T_e^M$ (blue dots). R is the
513 regression coefficient. (b) T_e reduction as a function of trench relief and breaking distance x_r.
514
515 **Figure 8.** (a) Averaged shapes of modeled best-fitting flexural bending profiles along the
516 Mariana trench for four ranges of axial vertical force (-V_0). (b) Averaged shapes of modeled best-
517 fitting flexural bending profiles for four ranges of axial bending moment (-M_0). (c) Range of
518 profiles with seamounts near the trench axis (stripe) in comparison to profiles with relatively
519 small (red) and large (green) axial vertical force. (d) Range of profiles with seamounts near the
520 trench axis (stripe) in comparison to profiles with relatively small (green) and large (red) axial
521 bending moment.
522
523 **Figure 9.** Map of shaded relief of the Mariana trench. Red curves mark the location of the trench
524 axis, while blue curves illustrate the calculated location of the transition from maximum to
525 minimum elastic thickness (x_r). Areas lack of high-resolution multi-beam bathymetry data are
526 marked by light green shades. Inset maps (a) and (b) show enlarged areas near the southern

Mariana trench. Note the general good correlation between x_r (blue curves) and the seaward boundary of the observed pervasive trench-parallel normal faults.

530 Table 1. Constant Parameters

Symbol	*Description*	*Value*	*Unit*
E	Young's modulus	7×10^{10}	Pa
g	Acceleration due to gravity	9.81	m s^{-2}
ν	Poisson's ratio	0.25	
ρ_m	Mantle density	3,300	kg m^{-3}
ρ_s	Sediment density	2,000	kg m^{-3}
ρ_c	Crust density	2,700	kg m^{-3}
ρ_w	Water density	1,030	kg m^{-3}

531

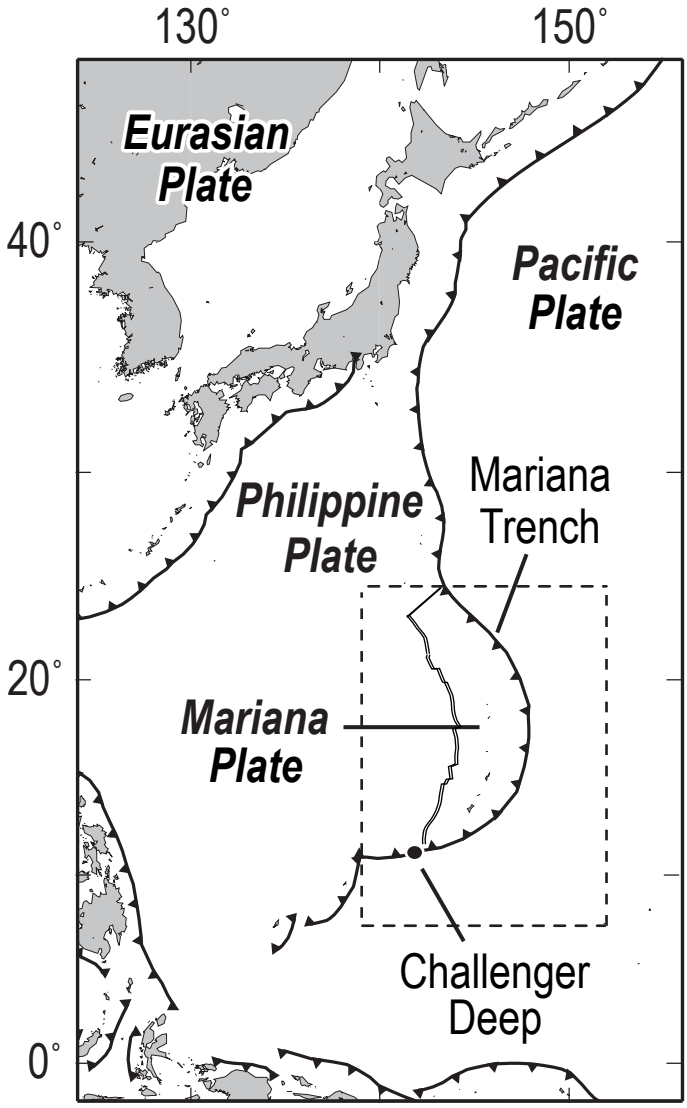
130˚
150˚
40˚
20˚
0˚
Eurasian Plate
Pacific Plate
Philippine Plate
Mariana Trench
Mariana Plate
Challenger Deep

Fig. 1

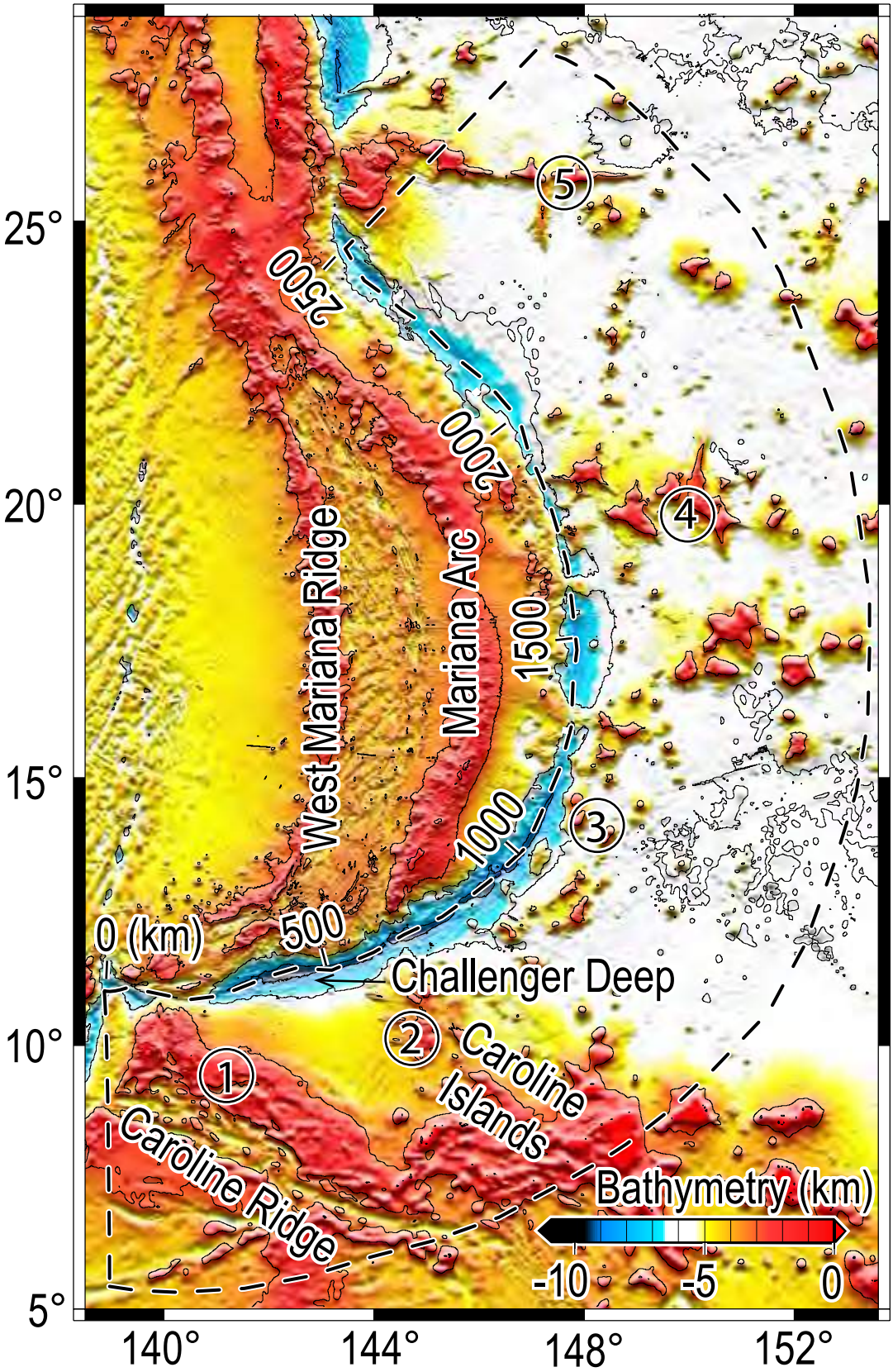
25°
20°
15°
10°
5°
140°
144°
148°
152°
500
1000
1500
2000
2500
West Mariana Ridge
Mariana Arc
0 (km)
Challenger Deep
Caroline Islands
Caroline Ridge
1
2
3
4
5
Bathymetry (km)
-10
-5
0

Fig. 2

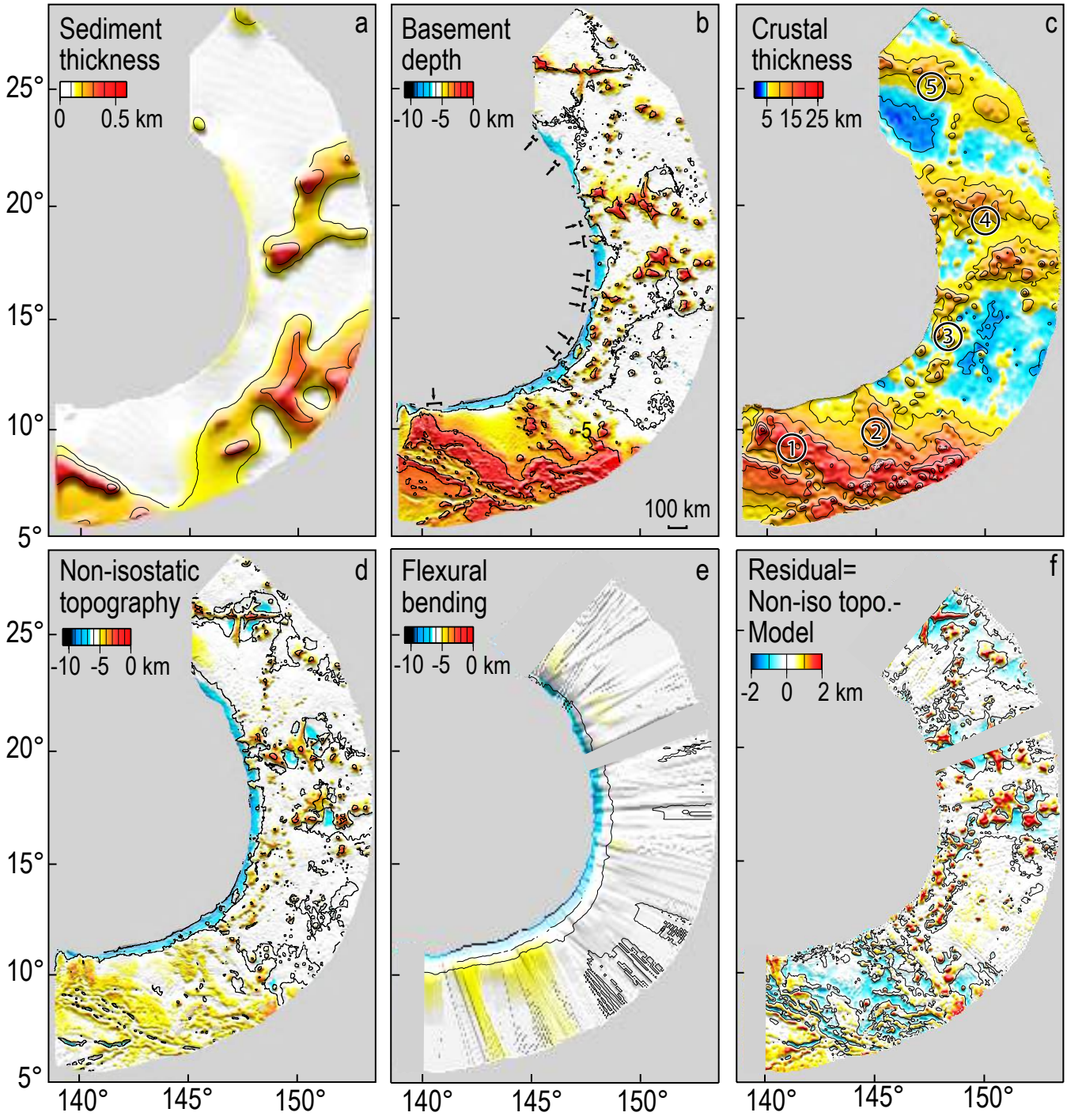
Sediment thickness
a
0 0.5 km
Basement depth
b
-10 -5 0 km
100 km
Crustal thickness
c
5 15 25 km
1
2
3
4
5
Non-isostatic topography
d
-10 -5 0 km
Flexural bending
e
-10 -5 0 km
Residual= Non-iso topo.- Model
f
-2 0 2 km
25°
20°
15°
10°
5°
140°
145°
150°

Fig. 3

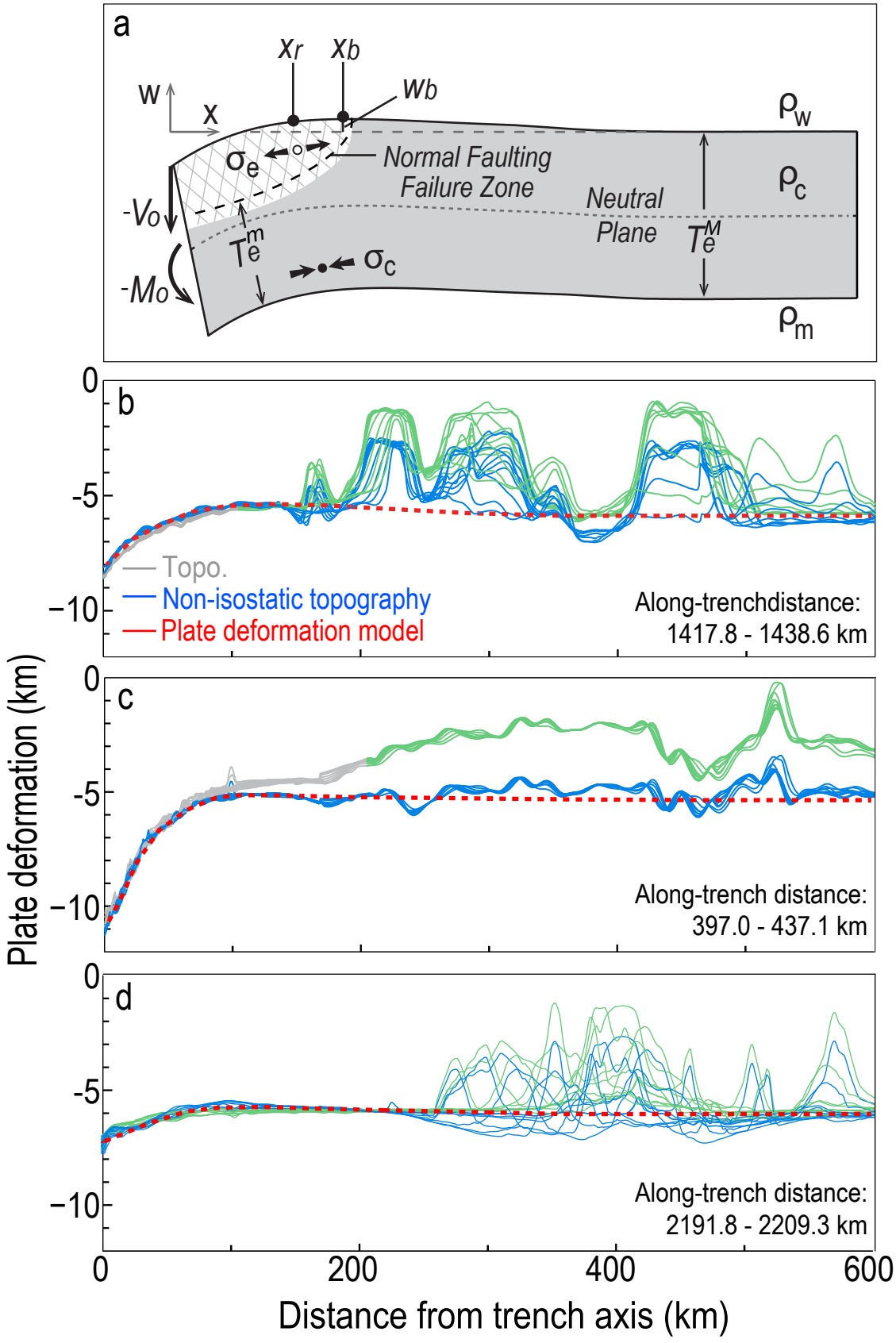
a
xr
xb
wb
w
x
ρw
σe
Normal Faulting
Failure Zone
ρc
Neutral
Plane
-Vo
Te^m
Te^M
σc
-Mo
ρm
b
Topo.
Non-isostatic topography
Plate deformation model
Along-trenchdistance:
1417.8 - 1438.6 km
c
Along-trench distance:
397.0 - 437.1 km
d
Along-trench distance:
2191.8 - 2209.3 km
Plate deformation (km)
0
-5
−10
0
200
400
600
Distance from trench axis (km)

Fig. 4

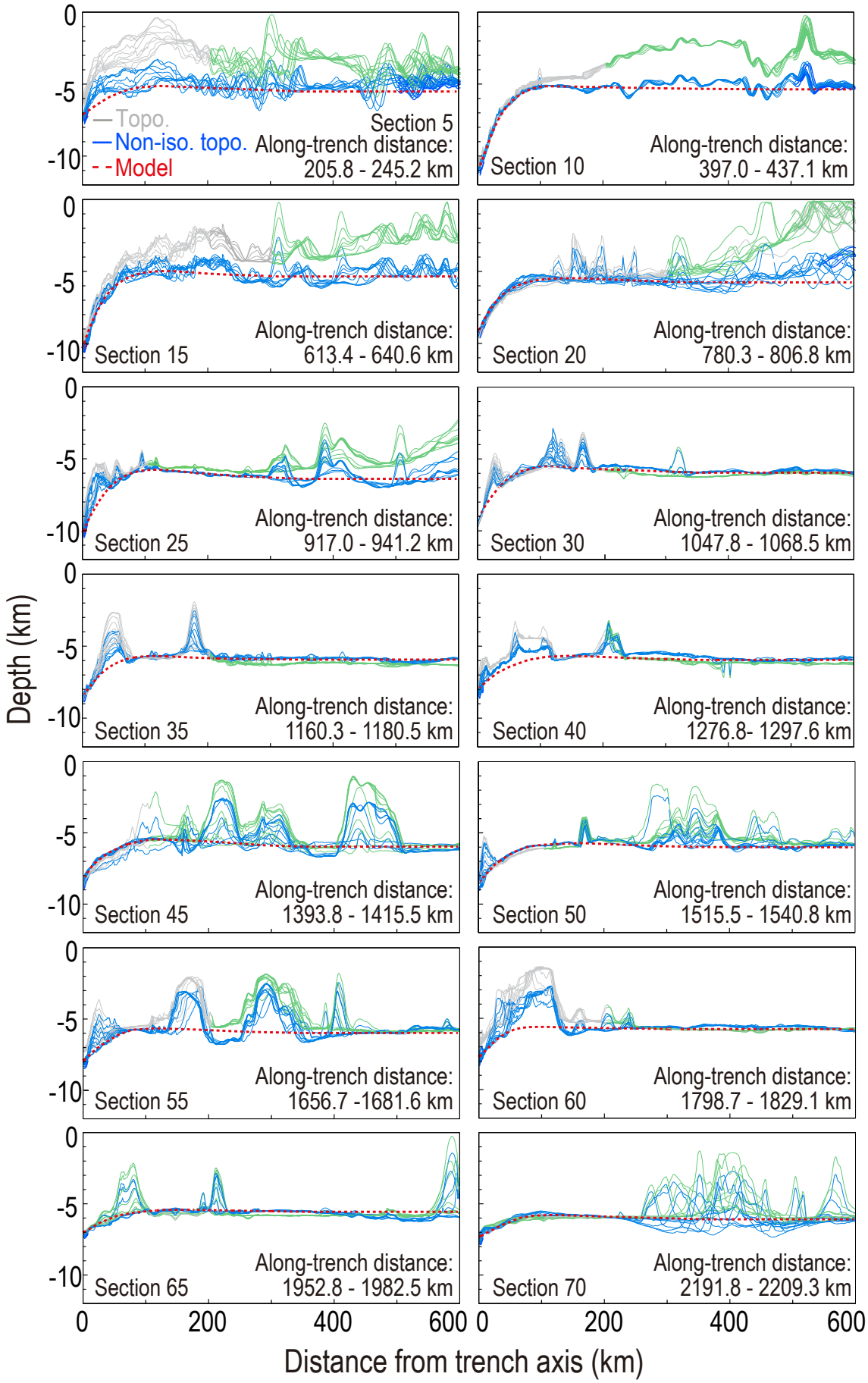
Topo.
Non-iso. topo.
Model
Section 5
Along-trench distance:
205.8 - 245.2 km
Section 10
Along-trench distance:
397.0 - 437.1 km
Section 15
Along-trench distance:
613.4 - 640.6 km
Section 20
Along-trench distance:
780.3 - 806.8 km
Section 25
Along-trench distance:
917.0 - 941.2 km
Section 30
Along-trench distance:
1047.8 - 1068.5 km
Section 35
Along-trench distance:
1160.3 - 1180.5 km
Section 40
Along-trench distance:
1276.8- 1297.6 km
Section 45
Along-trench distance:
1393.8 - 1415.5 km
Section 50
Along-trench distance:
1515.5 - 1540.8 km
Section 55
Along-trench distance:
1656.7 -1681.6 km
Section 60
Along-trench distance:
1798.7 - 1829.1 km
Section 65
Along-trench distance:
1952.8 - 1982.5 km
Section 70
Along-trench distance:
2191.8 - 2209.3 km
0
-5
-10
0
200
400
600
Depth (km)
Distance from trench axis (km)

Fig. 5

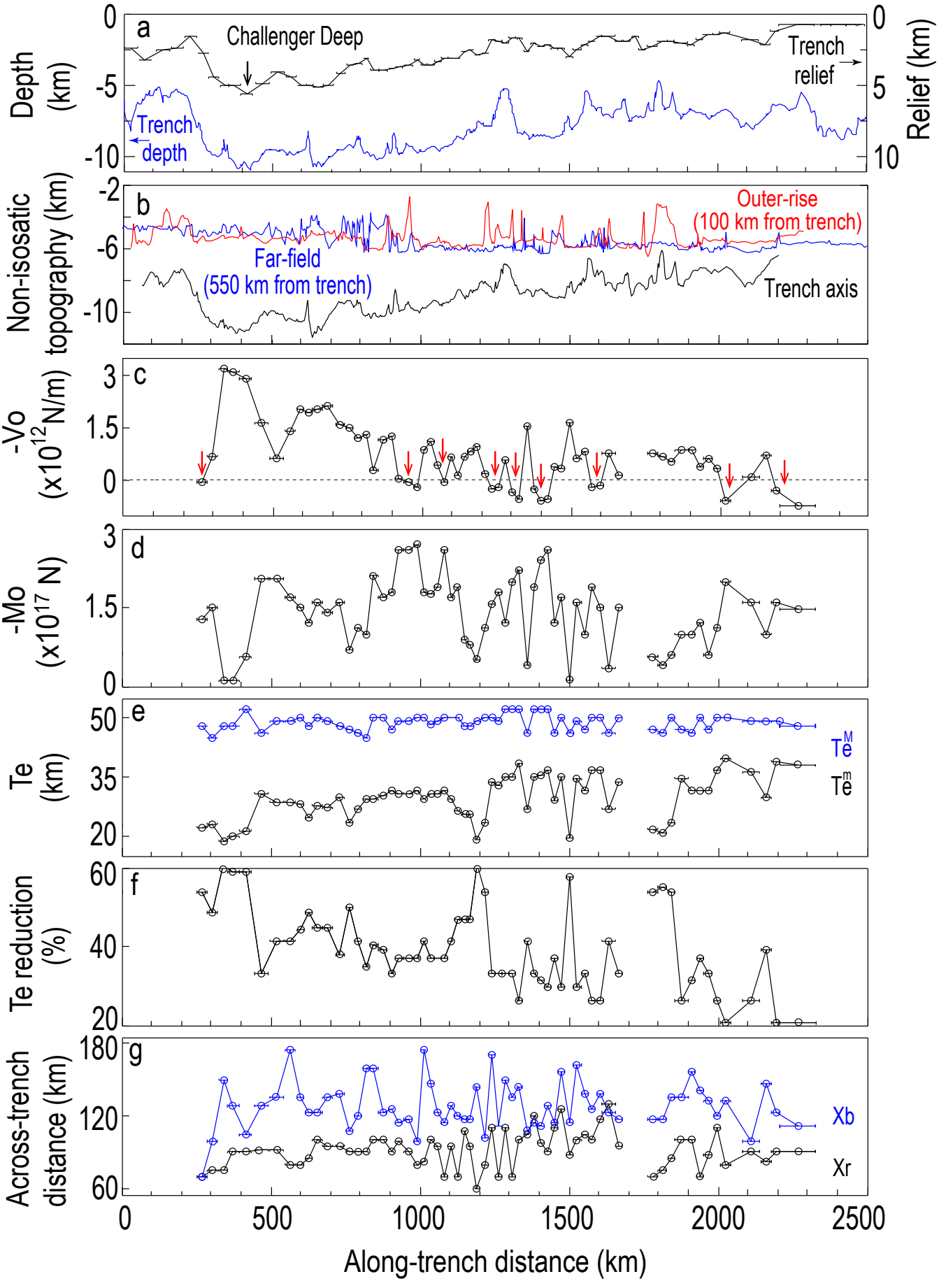
a
Challenger Deep
Trench relief
Trench depth
Depth (km)
Relief (km)
b
Outer-rise (100 km from trench)
Far-field (550 km from trench)
Trench axis
Non-isosatic topography (km)
c
-Vo (x10^12 N/m)
d
-Mo (x10^17 N)
e
Te (km)
Te^M
Te^m
f
Te reduction (%)
g
Across-trench distance (km)
Xb
Xr
Along-trench distance (km)

Fig. 6

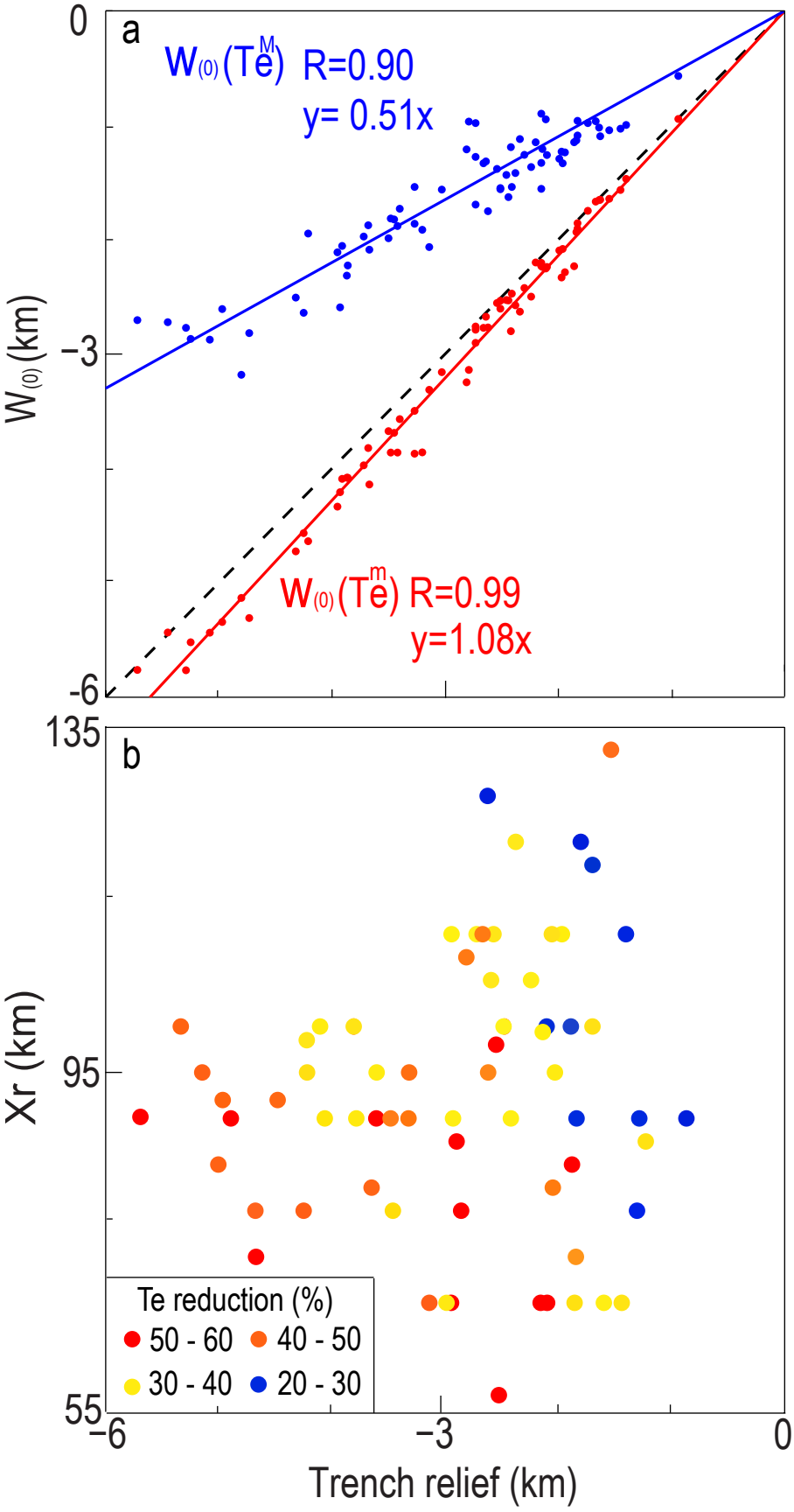
a
$W_{(0)}(Te^{M})$ R=0.90
y= 0.51x
$W_{(0)}(Te^{m})$ R=0.99
y=1.08x
$W_{(0)}$ (km)
0
−3
-6
b
Xr (km)
135
95
55
Te reduction (%)
50 - 60
40 - 50
30 - 40
20 - 30
−6
−3
0
Trench relief (km)

Fig. 7

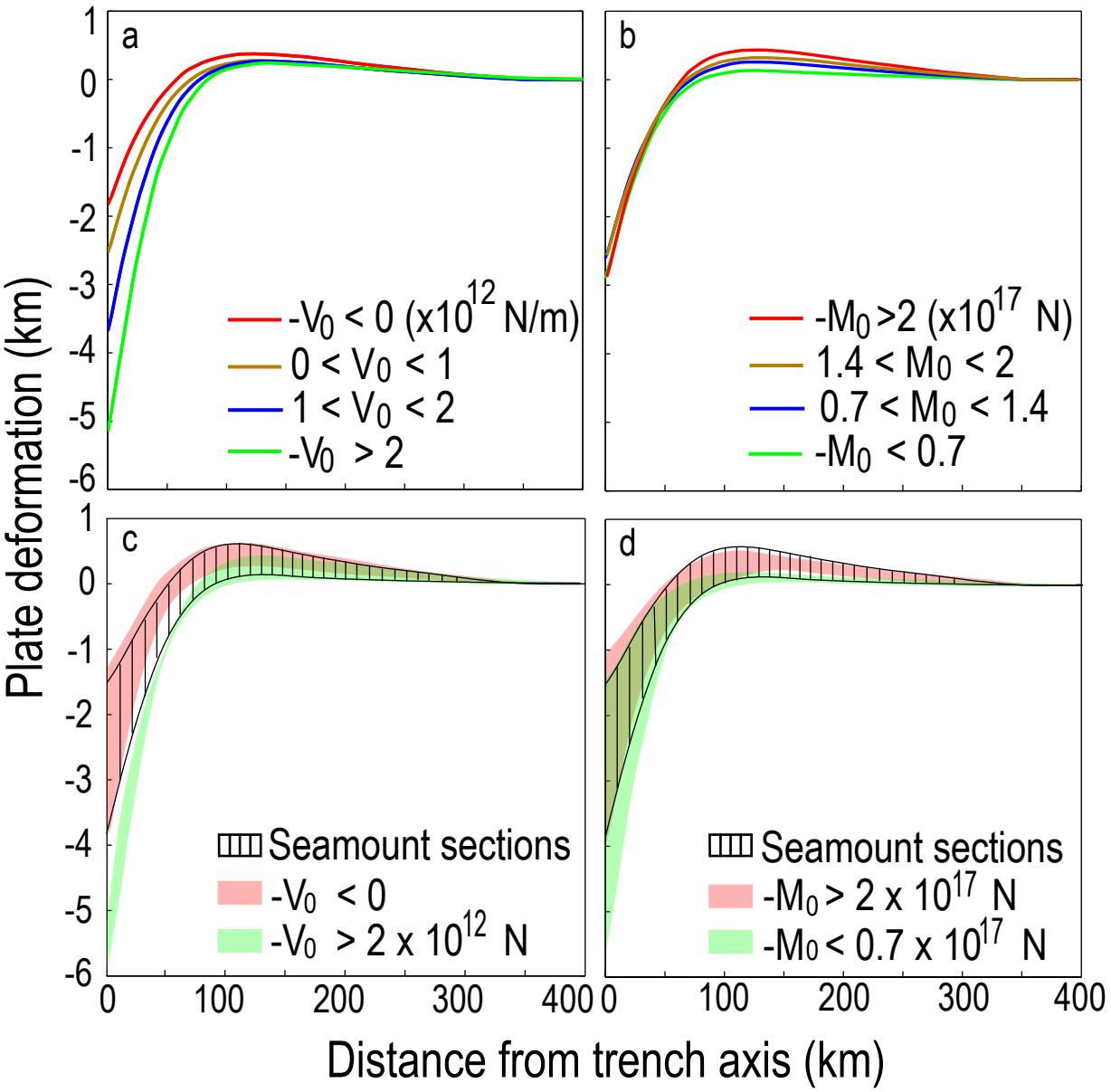
a
b
c
d
Plate deformation (km)
Distance from trench axis (km)
-V0 < 0 (x10^12 N/m)
0 < V0 < 1
1 < V0 < 2
-V0 > 2
-M0 >2 (x10^17 N)
1.4 < M0 < 2
0.7 < M0 < 1.4
-M0 < 0.7
Seamount sections
-V0 < 0
-V0 > 2 x 10^12 N
Seamount sections
-M0 > 2 x 10^17 N
-M0 < 0.7 x 10^17 N
1
0
-1
-2
-3
-4
-5
-6
0
100
200
300
400

Fig. 8

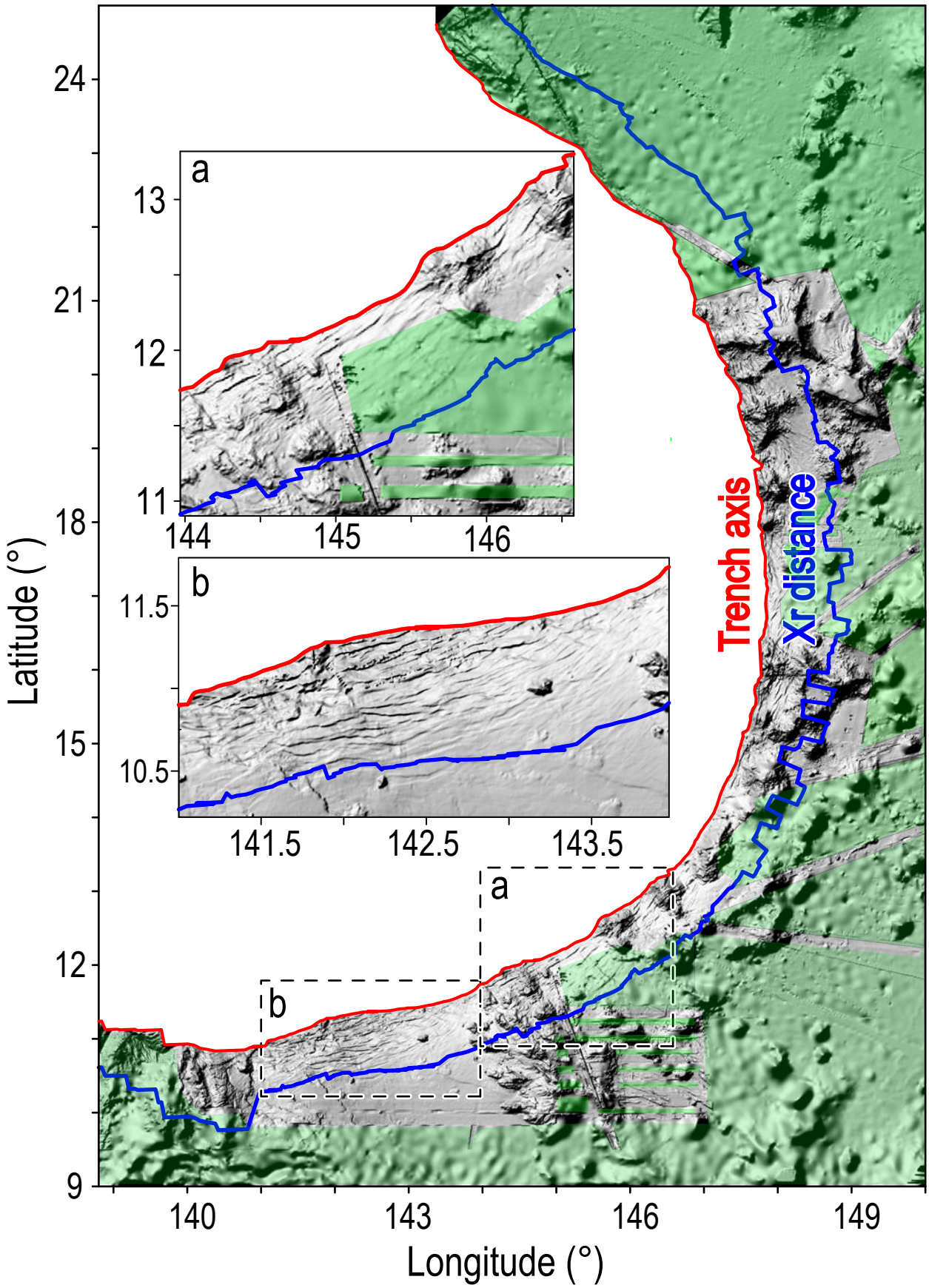
24
21
18
15
12
9
Latitude (°)
140
143
146
149
Longitude (°)
Trench axis
Xr distance
a
13
12
11
144
145
146
b
11.5
10.5
141.5
142.5
143.5
a
b

Fig. 9

Supplementary Materials

Supplementary Table 1. Best-Fitting Parameters for 75 Profile Sections

Section	Along-trench distance (km)	Trench relief (km)	$-V_0$ (10^{12} N/m)	$-M_0$ (10^{17} N)	T_e^m (km)	T_e^M (km)	x_r (km)	w_b (m)	T_e Reduction (%)
1*	0 - 48.8	-2.38	(0.84)	(0.63)	(22.7)	(49)	(70)	(142)	(53.6)
2*	53.1- 92.9	-3.36	(1.09)	(1.00)	(25.5)	(48)	(90)	(245)	(46.9)
3*	97.2 - 155.6	-2.59	(0.68)	(1.00)	(28.0)	(50)	(110)	(296)	(44.1)
4*	160.0 - 201.5	-2.47	(0.06)	(2.10)	(36.6)	(52)	(110)	(451)	(29.5)
5*	205.8 - 245.2	-1.69	(-0.30)	(1.80)	(38.1)	(54)	(120)	(385)	(29.5)
6	250.0 - 285.1	-2.74	-0.07	1.28	22.3	48	70	330	53.6
7	287.4 - 321.9	-4.16	0.69	1.50	23.1	45	75	417	48.7
8	326.0 - 357.2	-5.23	3.17	0.10	18.8	48	75	70	60.9
9	360.0 - 393.6	-5.40	3.11	0.10	18.8	48	85	141	60.9
10	397.0 - 437.1	-5.67	2.89	0.50	21.1	49	90	221	56.9
11	442.0 - 492.2	-4.76	1.62	2.05	30.8	46	92	311	33.1
12	498.1 - 541.8	-3.92	0.61	2.05	29.2	50	92	481	41.5
13	545.6 - 580.2	-4.28	1.41	1.85	29.2	50	82	350	41.5
14	583.4 - 611.1	-4.68	2.04	1.50	28.1	48	80	290	41.5
15	613.4 - 640.6	-4.94	1.93	1.20	24.6	48	85	352	48.7
16	643.4 - 670.5	-5.20	2.01	1.60	27.7	50	100	413	44.6
17	674.0 - 709.8	-5.05	2.13	1.40	27.1	49	95	368	44.6
18	717.4 - 746.7	-4.21	1.59	1.60	29.8	48	95	383	37.9
19	749.7 - 777.2	-3.63	1.50	0.70	23.5	47	90	232	50.0
20	780.3 - 806.8	-3.44	1.19	1.10	26.9	46	90	287	31.5
21*	809.1 - 829.4	-3.08	1.32	1.00	29.3	45	90	260	35.0
22*	831.9 - 859.9	-3.43	0.27	2.00	29.7	50	100	371	40.6
23	862.9 - 889.3	-3.82	1.14	1.70	30.4	50	100	343	39.2
24	891.8 - 914.7	-3.89	1.27	1.80	31.5	47	90	374	33.1
25*	917.0 – 941.2	-3.85	0.03	2.60	30.9	49	99	650	37.0
26*	945.1 - 975.7	-3.67	-0.07	2.60	30.9	49	90	603	37.0
27*	978.1- 999.9	-3.38	-0.20	2.70	31.5	50	80	528	37.0
28*	1002.3 - 1022.7	-3.64	0.88	1.80	29.2	50	83	287	41.5
29*	1024.9 -1045.5	-3.82	1.10	1.75	30.6	48	100	394	37.0
30*	1047.8 -1068.5	-3.22	0.45	1.90	30.9	49	95	448	37.0
31	1070.8 - 1090.9	-3.15	-0.07	2.60	31.5	50	70	517	37.0
32	1093.1 - 1111.1	-3.40	0.65	1.70	29.2	50	95	373	41.5
33	1115.3 - 1135.7	-3.21	0.12	1.90	26.6	50	70	408	46.9
34*	1138.1 - 1158.1	-2.68	0.65	0.90	25.5	48	108	326	46.9
35*	1160.3 - 1180.5	-2.60	0.81	0.80	25.5	48	95	267	46.9
36	1182.7 - 1202.9	-2.75	0.98	0.50	19.2	49	60	164	60.9
37*	1205.3 - 1227.3	-2.68	0.18	1.10	23.2	50	80	316	53.6
38*	1229.6 - 1250.2	-1.77	-0.27	1.55	33.5	50	110	307	33.1
39*	1252.6 - 1274.3	-1.92	-0.21	1.80	32.8	49	70	314	33.1
40	1276.8 - 1297.6	-2.09	0.59	1.20	34.8	52	110	288	33.1
41*	1300.0 - 1321.5	-1.80	-0.35	2.00	34.8	52	70	385	33.1
42*	1323.9 - 1345.5	-1.79	-0.55	2.20	38.3	52	100	366	26.3
43	1347.8 - 1368.7	-2.67	1.54	0.40	26.9	46	105	131	41.5
44*	1371.1 - 1391.4	-2.14	-0.26	1.90	34.8	52	120	450	33.1
45	1393.8 - 1415.5	-2.24	-0.57	2.40	35.6	52	98	514	31.6
46*	1417.8 - 1438.6	-2.33	-0.55	2.60	36.6	52	90	509	29.5
47	1441.3 - 1463.6	-2.48	0.40	1.20	29.0	46	110	421	37.0
48*	1465.9 - 1487.3	-2.46	0.33	1.70	35.2	50	125	368	29.5
49	1490.0 - 1512.8	-2.99	1.66	0.13	19.9	47	90	82	57.6
50*	1515.5 - 1540.8	-2.58	0.60	1.60	34.5	49	100	303	29.5
51	1543.0 - 1563.4	-2.35	0.82	1.00	31.5	47	105	233	33.1
52*	1565.8 - 1590.8	-1.95	-0.18	1.90	36.8	50	100	328	26.3
53*	1599.3 - 1610.0	-1.60	-0.14	1.50	36.8	50	117	332	26.3
54	1618.5 - 1654.4	-1.62	0.76	0.50	30.6	50	110	186	38.7
55*	1656.7 - 1681.6	-2.05	0.15	1.50	33.5	50	95	325	33.1
56*	1683.9 - 1709.2	-2.09	(-0.10)	(1.70)	(33.5)	(50)	(100)	(384)	(33.1)
57*	1712.1 - 1736.0	-1.79	(0.22)	(1.20)	(33.5)	(46)	(100)	(280)	(33.1)
58*	1738.2 - 1760.4	-2.40	(1.05)	(0.60)	(26.9)	(46)	(100)	(179)	(31.5)

59*	1763.6 - 1796.3	-2.28	0.77	0.55	21.8	47	70	164	53.6
60*	1798.7 - 1829.1	-2.05	0.69	0.40	20.6	46	75	164	55.2
61*	1832.0 - 1857.7	-2.10	0.54	0.60	23.2	50	85	160	53.6
62	1860.5 - 1899.9	-2.10	0.84	1.00	34.6	46	100	242	31.2
63	1902.3 - 1923.1	-2.38	0.88	1.00	31.6	46	100	265	31.2
64*	1925.7 - 1949.9	-1.87	0.40	1.20	31.5	50	70	246	37.0
65*	1952.8 - 1982.5	-1.49	0.63	0.60	31.5	47	87	140	33.1
66	1984.9 - 2010.9	-1.57	0.32	1.10	36.8	50	110	234	26.3
67	2013.2 - 2044.7	-1.39	-0.59	2.00	39.7	50	80	349	20.6
68	2061.7 - 2138.6	-1.91	0.10	1.60	36.1	49	90	276	26.3
69	2142.6 - 2179.2	-2.20	0.70	1.00	29.8	49	83	176	39.2
70	2191.8 - 2209.3	-1.53	-0.30	1.60	36.1	49	90	306	26.3
71	2212.5 - 2328.9	-0.87	-0.73	1.48	38.1	48	90	326	20.6
72	2341.7 - 2382.3	-	-	-	-	-	-	-	-
73	2384.6 - 2432.5	-	-	-	-	-	-	-	-
74	2436.9 - 2469.5	-	-	-	-	-	-	-	-
75	2472.5 - 2495.5	-	-	-	-	-	-	-	-

Notes:
- The star symbol (*) marks sections with seamounts near the trench axis.
- Parameters bracketed with parentheses, i.e., Sections 1-5 and 56-58, are relatively poorly constrained due to significant effects of seamounts near the profile sections.
- For Sections 72-75, sediment thickness data are not available and thus several parameters were not calculated.

Appendix A. Topography and Flexural Bending of 75 Profile Sections of the Mariana Trench

We analyzed flexural bending along 75 across-trench sections, each consists of ten profiles spanning over an along-trench distance of about 0.2° (Figs. S1-8). For each profile section, we calculated a flexural bending model that best matches non-isostatic topography (blue curves) of areas away from seamounts.

Figure Captions

Figure S1-8. A total of 75 across-trench profile sections of the Mariana trench. Basement topography of every ten individual profiles was stacked to form an averaged section for modeling: grey and green curves show areas with and without multi-beam bathymetry, respectively. Blue curves are the calculated non-isostatic topography. Red dashed curves show flexural bending models that best fit non-isostatic topography away from seamounts.

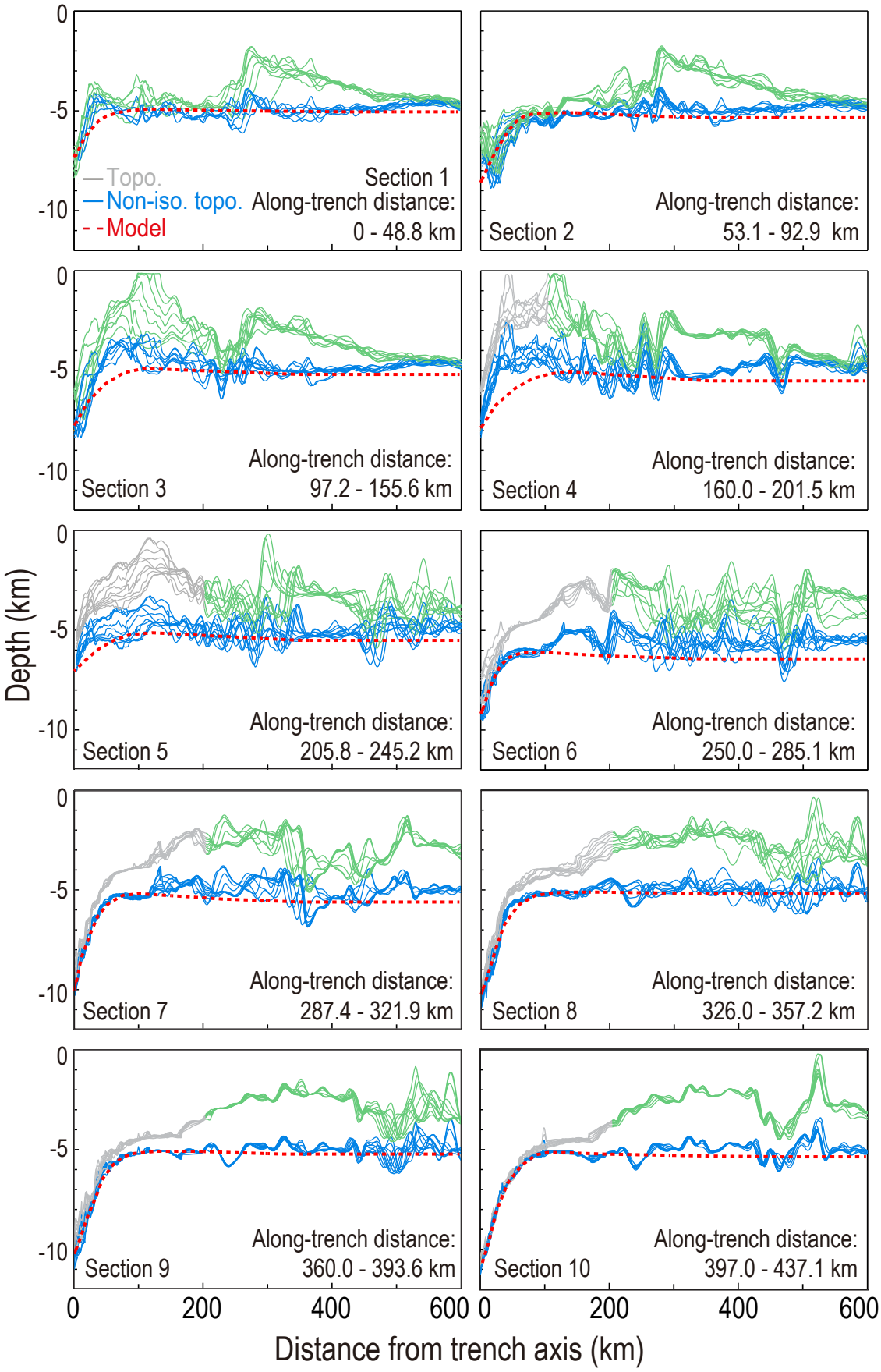
Topo.
Non-iso. topo.
Model
Section 1
Along-trench distance:
0 - 48.8 km
Section 2
Along-trench distance:
53.1 - 92.9 km
Section 3
Along-trench distance:
97.2 - 155.6 km
Section 4
Along-trench distance:
160.0 - 201.5 km
Section 5
Along-trench distance:
205.8 - 245.2 km
Section 6
Along-trench distance:
250.0 - 285.1 km
Section 7
Along-trench distance:
287.4 - 321.9 km
Section 8
Along-trench distance:
326.0 - 357.2 km
Section 9
Along-trench distance:
360.0 - 393.6 km
Section 10
Along-trench distance:
397.0 - 437.1 km
Depth (km)
0
-5
-10
0
200
400
600
Distance from trench axis (km)

Fig. S1

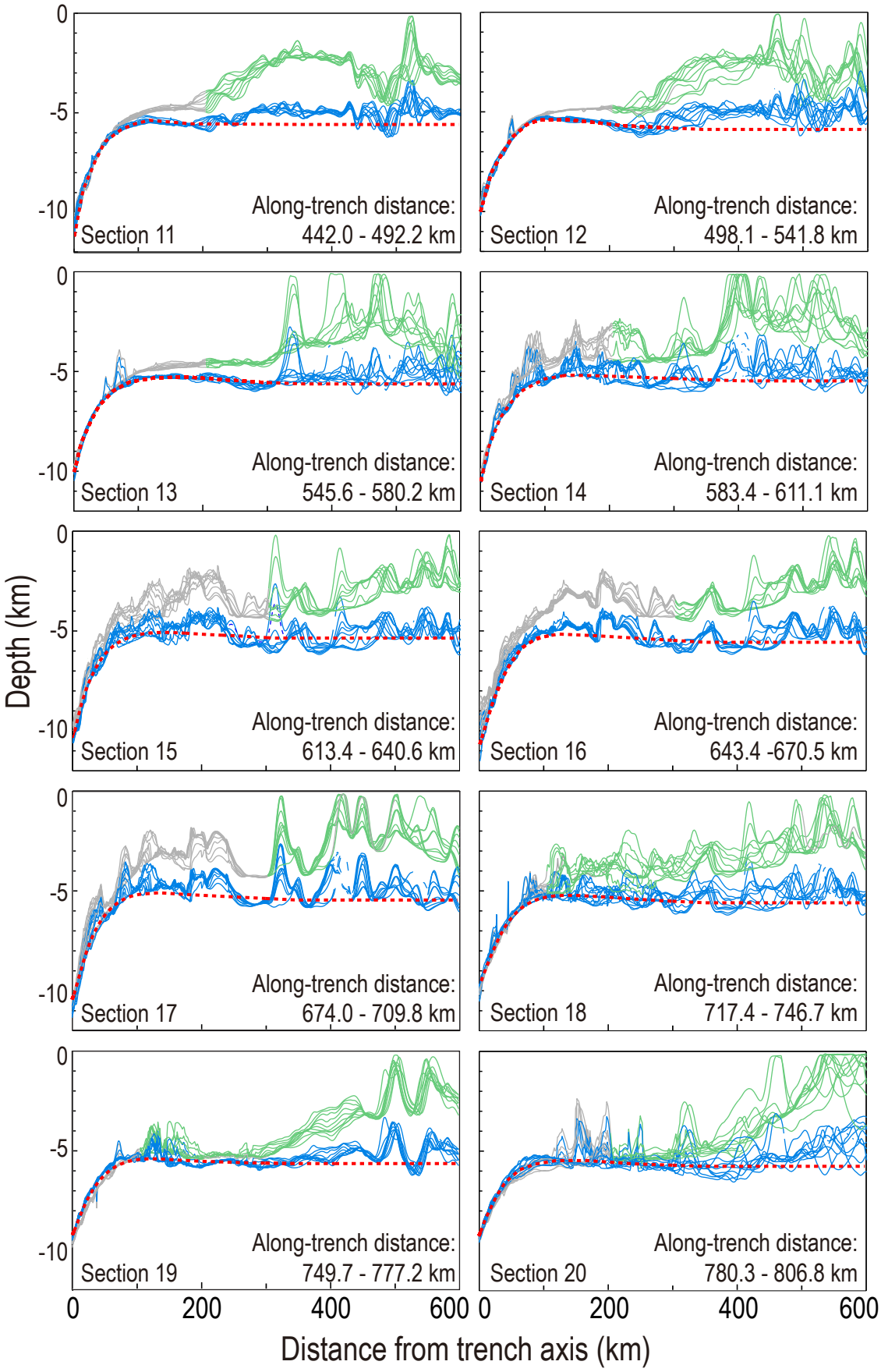
Depth (km)
0
-5
-10
Section 11
Along-trench distance:
442.0 - 492.2 km
Section 12
Along-trench distance:
498.1 - 541.8 km
Section 13
Along-trench distance:
545.6 - 580.2 km
Section 14
Along-trench distance:
583.4 - 611.1 km
Section 15
Along-trench distance:
613.4 - 640.6 km
Section 16
Along-trench distance:
643.4 -670.5 km
Section 17
Along-trench distance:
674.0 - 709.8 km
Section 18
Along-trench distance:
717.4 - 746.7 km
Section 19
Along-trench distance:
749.7 - 777.2 km
Section 20
Along-trench distance:
780.3 - 806.8 km
0
200
400
600
Distance from trench axis (km)

Fig. S2

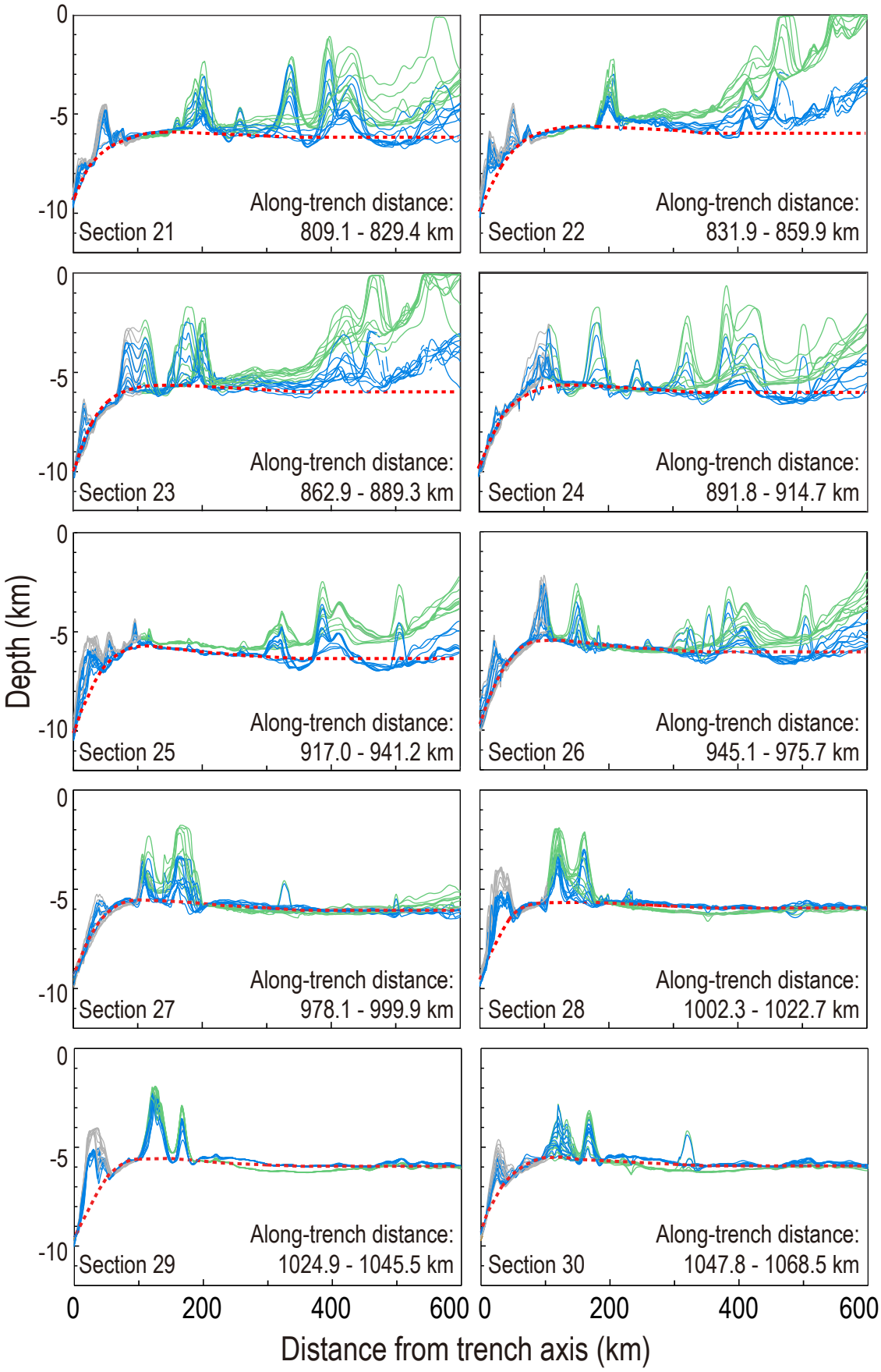
Depth (km)
0
-5
-10
Section 21
Along-trench distance:
809.1 - 829.4 km
Section 22
Along-trench distance:
831.9 - 859.9 km
Section 23
Along-trench distance:
862.9 - 889.3 km
Section 24
Along-trench distance:
891.8 - 914.7 km
Section 25
Along-trench distance:
917.0 - 941.2 km
Section 26
Along-trench distance:
945.1 - 975.7 km
Section 27
Along-trench distance:
978.1 - 999.9 km
Section 28
Along-trench distance:
1002.3 - 1022.7 km
Section 29
Along-trench distance:
1024.9 - 1045.5 km
Section 30
Along-trench distance:
1047.8 - 1068.5 km
0
200
400
600
Distance from trench axis (km)

Fig. S3

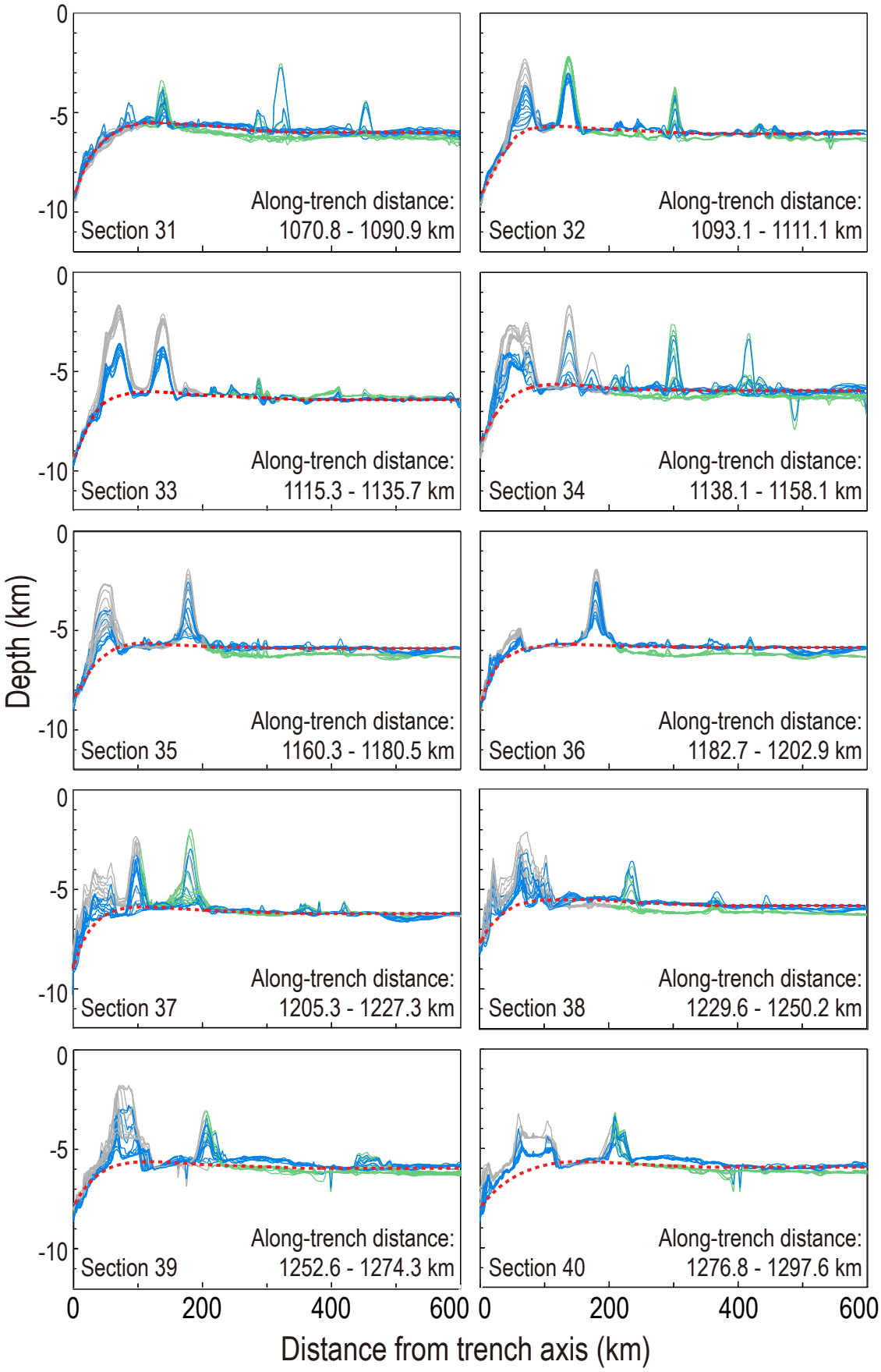
Depth (km)
0
-5
-10
Section 31
Along-trench distance:
1070.8 - 1090.9 km
Section 32
Along-trench distance:
1093.1 - 1111.1 km
Section 33
Along-trench distance:
1115.3 - 1135.7 km
Section 34
Along-trench distance:
1138.1 - 1158.1 km
Section 35
Along-trench distance:
1160.3 - 1180.5 km
Section 36
Along-trench distance:
1182.7 - 1202.9 km
Section 37
Along-trench distance:
1205.3 - 1227.3 km
Section 38
Along-trench distance:
1229.6 - 1250.2 km
Section 39
Along-trench distance:
1252.6 - 1274.3 km
Section 40
Along-trench distance:
1276.8 - 1297.6 km
0
200
400
600
Distance from trench axis (km)

Fig. S4

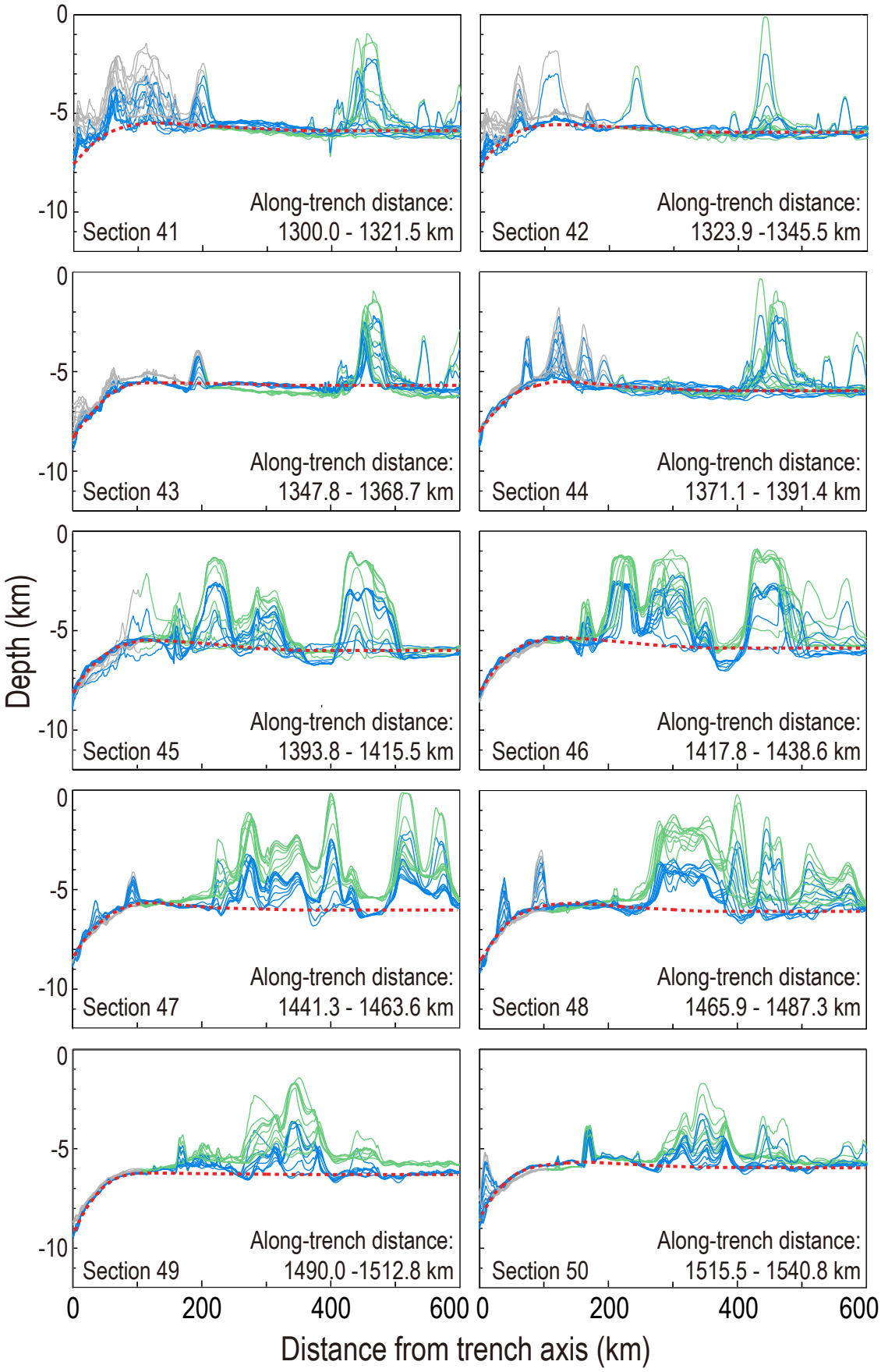
Depth (km)
0
-5
-10
Section 41
Along-trench distance:
1300.0 - 1321.5 km
Section 42
Along-trench distance:
1323.9 -1345.5 km
Section 43
Along-trench distance:
1347.8 - 1368.7 km
Section 44
Along-trench distance:
1371.1 - 1391.4 km
Section 45
Along-trench distance:
1393.8 - 1415.5 km
Section 46
Along-trench distance:
1417.8 - 1438.6 km
Section 47
Along-trench distance:
1441.3 - 1463.6 km
Section 48
Along-trench distance:
1465.9 - 1487.3 km
Section 49
Along-trench distance:
1490.0 -1512.8 km
Section 50
Along-trench distance:
1515.5 - 1540.8 km
0
200
400
600
Distance from trench axis (km)

Fig. S5

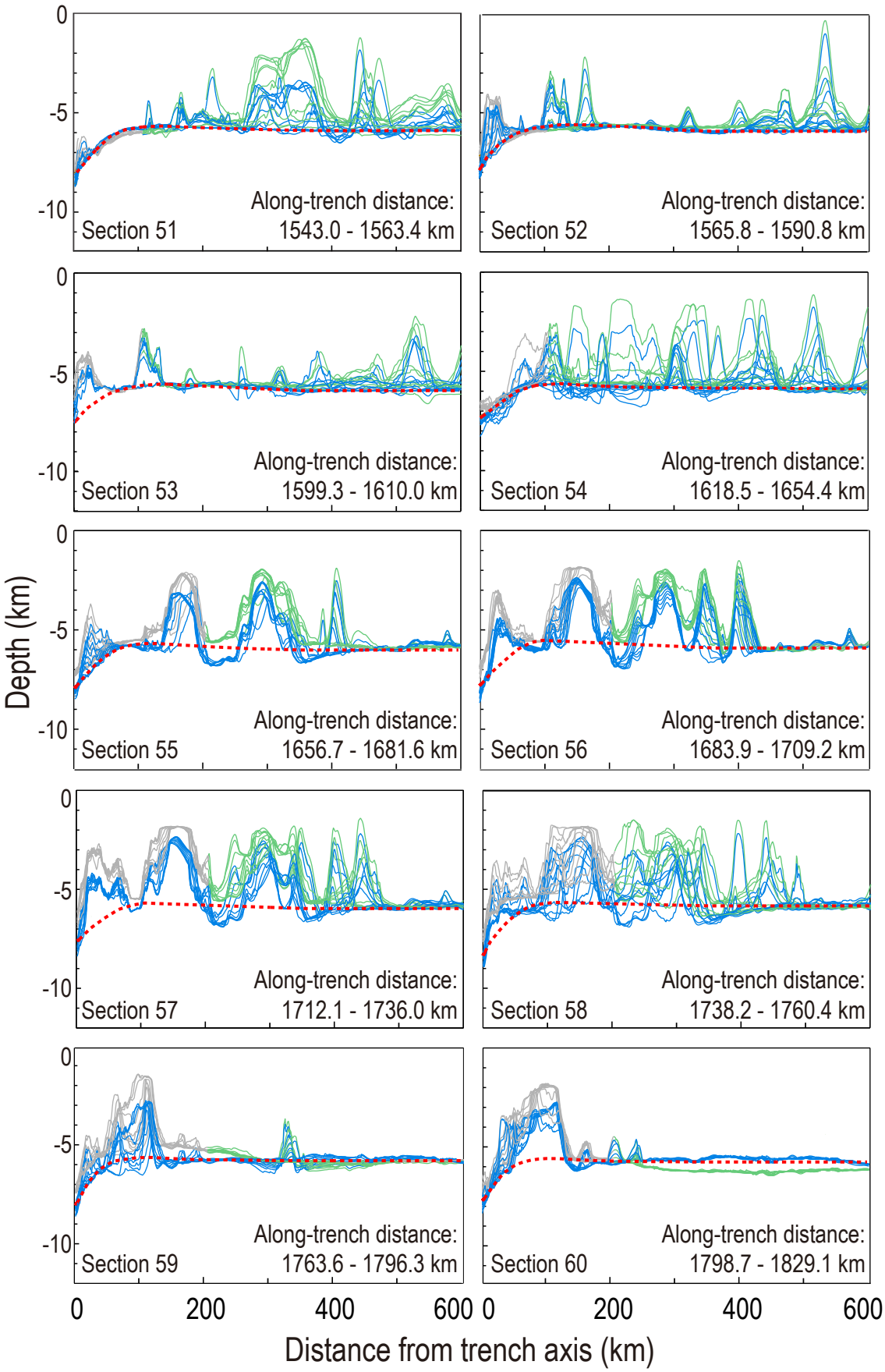
Depth (km)
0
-5
-10
Section 51
Along-trench distance:
1543.0 - 1563.4 km
Section 52
Along-trench distance:
1565.8 - 1590.8 km
Section 53
Along-trench distance:
1599.3 - 1610.0 km
Section 54
Along-trench distance:
1618.5 - 1654.4 km
Section 55
Along-trench distance:
1656.7 - 1681.6 km
Section 56
Along-trench distance:
1683.9 - 1709.2 km
Section 57
Along-trench distance:
1712.1 - 1736.0 km
Section 58
Along-trench distance:
1738.2 - 1760.4 km
Section 59
Along-trench distance:
1763.6 - 1796.3 km
Section 60
Along-trench distance:
1798.7 - 1829.1 km
0
200
400
600
Distance from trench axis (km)

Fig. S6

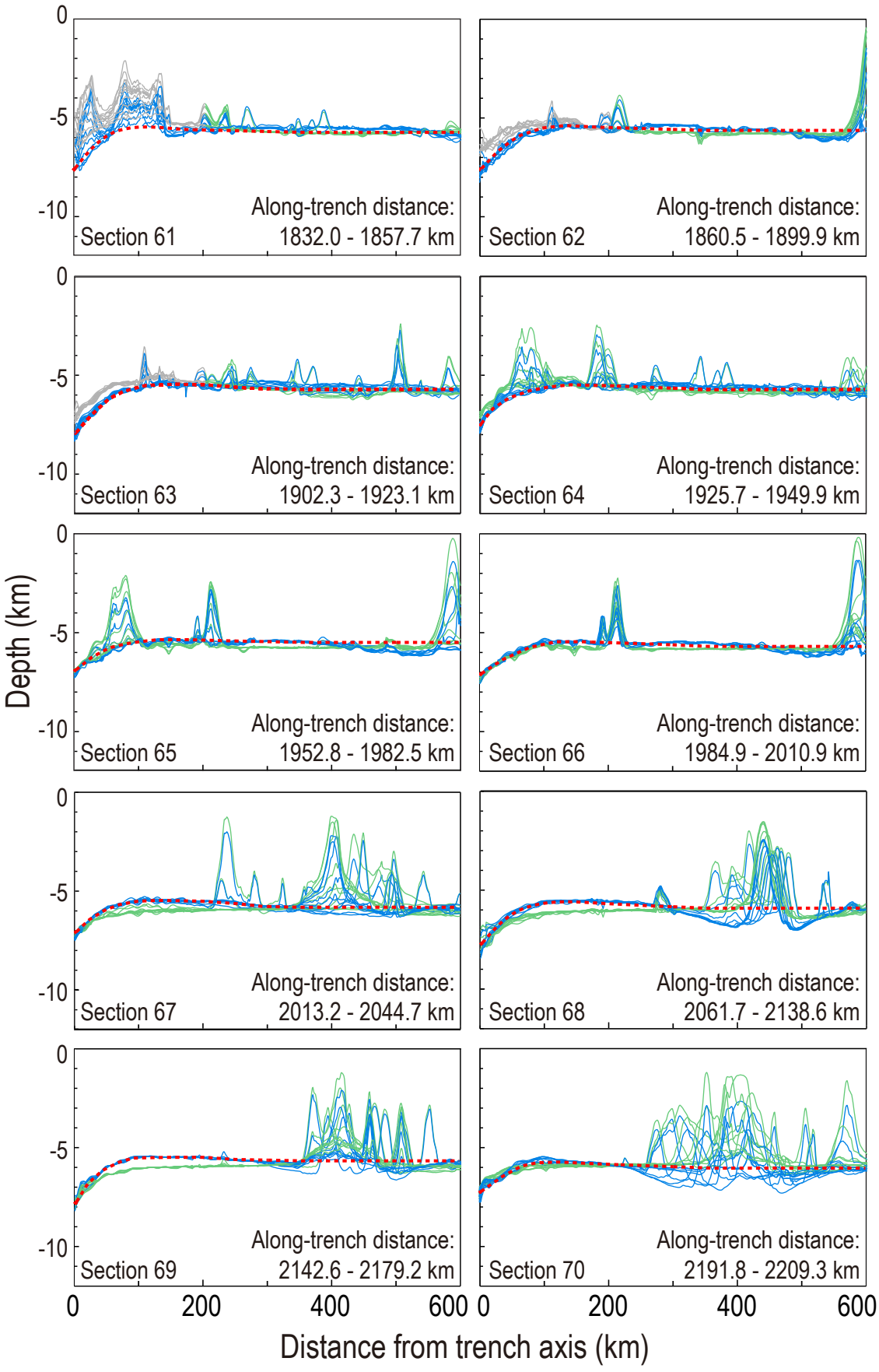
Depth (km)
0
-5
-10
Section 61
Along-trench distance:
1832.0 - 1857.7 km
Section 62
Along-trench distance:
1860.5 - 1899.9 km
Section 63
Along-trench distance:
1902.3 - 1923.1 km
Section 64
Along-trench distance:
1925.7 - 1949.9 km
Section 65
Along-trench distance:
1952.8 - 1982.5 km
Section 66
Along-trench distance:
1984.9 - 2010.9 km
Section 67
Along-trench distance:
2013.2 - 2044.7 km
Section 68
Along-trench distance:
2061.7 - 2138.6 km
Section 69
Along-trench distance:
2142.6 - 2179.2 km
Section 70
Along-trench distance:
2191.8 - 2209.3 km
0
200
400
600
Distance from trench axis (km)

Fig. S7

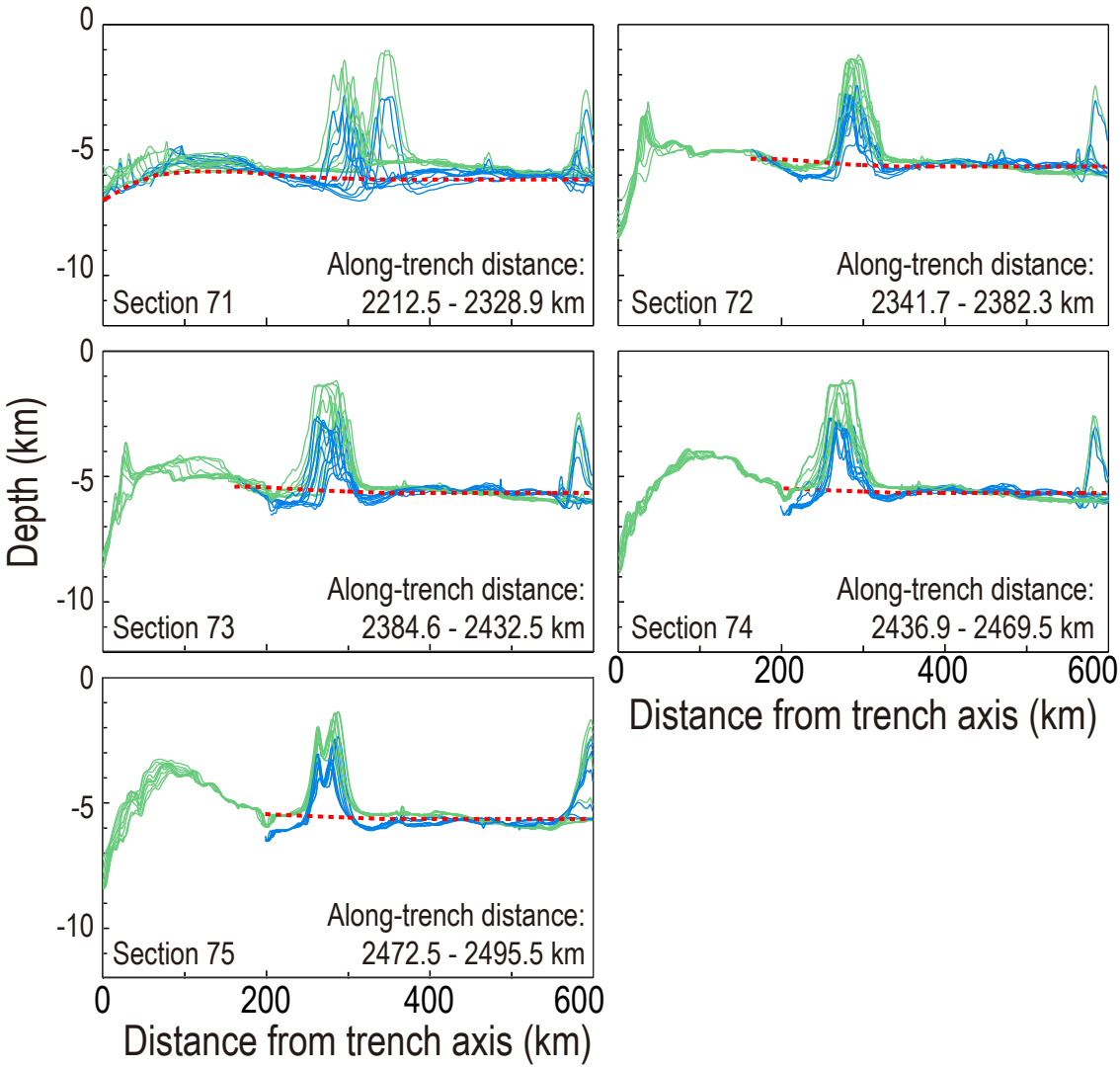
Depth (km)
0
-5
-10
Section 71
Along-trench distance:
2212.5 - 2328.9 km
Section 72
Along-trench distance:
2341.7 - 2382.3 km
Section 73
Along-trench distance:
2384.6 - 2432.5 km
Section 74
Along-trench distance:
2436.9 - 2469.5 km
Section 75
Along-trench distance:
2472.5 - 2495.5 km
0
200
400
600
Distance from trench axis (km)

Fig. S8

Appendix B. Numerical Solutions of Flexural Bending of a Plate with Variable Elastic Thickness

The flexural bending of a thin elastic plate is described by the following equation (Turcotte and Schubert, 2002):

$$-\frac{d^2M}{dx^2}+\frac{d}{dx}(F\frac{dw}{dx})+\Delta\rho gw=q\,, \tag{S1}$$

where $w(x)$ is vertical deflection of the plate, $M(x)$ is bending moment, $F(x)$ is horizontal buckling force, $\Delta\rho gw=(\rho_m-\rho_w)gw$ represents hydrostatic restoring force, $q(x)=(\rho_s-\rho_w)gh_s(x)$ is vertical sediment loading, $h_s(x)$ is sediment thickness, and ρ_w, ρ_s, and ρ_m are densities of water, sediment, and mantle, respectively.

Assuming that the spatial variation in the buckling force, $\frac{dF(x)}{dx}$, is relatively small, Eqn. S1 can be re-written as the following set of second-order differential equations (Contreras-Reyes and Osses, 2010):

$$\frac{d^2w}{dx^2}=-\frac{M}{D}\,; \tag{S2}$$

$$\frac{d^2M}{dx^2}=-F\frac{M}{D}+\Delta\rho gw-q\,, \tag{S3}$$

where flexural rigidity is $D(x)=\frac{ET_e(x)^3}{12(1-\nu^2)}$, while T_e, E, and ν are the effective elastic thickness of the plate, Young's modulus, and Poisson's ratio, respectively.

To solve for the four variables, w, $\frac{dw}{dx}$, M, and $\frac{dM}{dx}$, the above Eqns. S2 and S3 can be further re-written as a set of first-order differential equations in a matrix form:

$$\frac{d}{dx}\begin{pmatrix} w \\ \frac{dw}{dx} \\ M \\ \frac{dM}{dx} \end{pmatrix} + \begin{pmatrix} 0 & -1 & 0 & 0 \\ 0 & 0 & \frac{1}{D(x)} & 0 \\ 0 & 0 & 0 & -1 \\ -\Delta\rho g & 0 & \frac{F(x)}{D(x)} & 0 \end{pmatrix} \times \begin{pmatrix} w \\ \frac{dw}{dx} \\ M \\ \frac{dM}{dx} \end{pmatrix} = \begin{pmatrix} 0 \\ 0 \\ 0 \\ -q(x) \end{pmatrix} \quad \text{(S4)}$$

The above Eqn. S4 is then solved using the finite-difference method.

In finite-difference operation, the x domain of length L is discretized into N grid points of equal distance, i.e., $x(\mathrm{i}) = (\mathrm{i}-1)\Delta x$, for i=1:N, where $\Delta x = L/(\mathrm{N}-1)$. For grid points away from the boundary, i.e., for i=2:N-1, the four rows of the first-order differential equations in Eqn. S4 are described by the following:

$$\frac{dw(\mathrm{i})}{dx} = \frac{w(\mathrm{i}+1) - w(\mathrm{i}\text{-}1)}{2\Delta x}; \quad \text{(S5)}$$

$$\frac{dw(\mathrm{i}+1)/dx - dw(\mathrm{i}\text{-}1)/dx}{dx} + \frac{M(\mathrm{i})}{D(\mathrm{i})} = 0; \quad \text{(S6)}$$

$$\frac{dM(\mathrm{i})}{dx} = \frac{M(\mathrm{i}+1) - M(\mathrm{i}\text{-}1)}{2\Delta x}; \quad \text{(S7)}$$

$$\frac{dM(\mathrm{i}+1)/dx - dM(\mathrm{i}\text{-}1)/dx}{2\Delta x} - \Delta\rho g w(\mathrm{i}) + \frac{F(\mathrm{i})M(\mathrm{i})}{D(\mathrm{i})} = -q(\mathrm{i}). \quad \text{(S8)}$$

When applied to the grid points of i=2:N-1, Eqns. S5-S8 yield a total of 4N-8 constraints.

The boundary conditions at x=0 and x=L are prescribed as the following:

$$M=M_0,\ \frac{d^2M}{dx^2} = V_0 + F_0\frac{dw}{dx}, \text{ at x=0,} \quad \text{(S9)}$$

$$w=0,\ \frac{dw}{dx} = 0, \text{ at x=}L, \quad \text{(S10)}$$

where V_0, M_0, and F_0 are, respectively, the given vertical force, bending moment, and horizontal force at x=0.

The boundary conditions for Eqn. S4 can be further expressed in 8 sets of finite-difference operations:

$$\frac{dw(1)}{dx}=\frac{w(2)-w(1)}{\Delta x}; \tag{S11}$$

$$w(\mathrm{N})=0; \tag{S12}$$

$$\frac{dw(2)/dx-dw(1)/dx}{\Delta x}+\frac{M_0}{D_0}=0; \tag{S13}$$

$$\frac{-dw(\mathrm{N}-1)/dx}{dx}+\frac{M(\mathrm{N})}{D(\mathrm{N})}=0; \tag{S14}$$

$$\frac{dM(1)}{dx}=\frac{M(2)-M_0}{\Delta x}; \tag{S15}$$

$$\frac{dM(\mathrm{N})}{dx}=\frac{M(\mathrm{N})-M(\mathrm{N}\text{-}1)}{\Delta x}; \tag{S16}$$

$$\frac{dM(2)/dx-dM(1)/dx}{\Delta x}-\Delta\rho g w(1)+\frac{F_0M_0}{D_0}=-q(1); \tag{S17}$$

$$\frac{dM(\mathrm{N})/dx-dM(\mathrm{N}\text{-}1)/dx}{\Delta x}-\Delta\rho g w(\mathrm{N})+\frac{F(\mathrm{N})M(\mathrm{N})}{D(\mathrm{N})}=-q(\mathrm{N}); \tag{S18}$$

Eqns. S11-S18 yield a total of 8 constraints. In sum, Eqns. S5-S8 together with Eqns. S11-S18 provide a total of 4N constraints, which are used through matrix inversion to solve for the 4N unknowns of $w(\mathrm{i})$, $\frac{dw(\mathrm{i})}{dx}$, $M(\mathrm{i})$, and $\frac{dM(\mathrm{i})}{dx}$, for i=1:N.

Appendix C. Gravity-Derived Crustal Thickness

We used gravity-derived crustal thickness (Fig. 3c) to calculate isostatic topography. The crustal thickness for the study region was calculated by following steps:

(1) *Data and Analysis.* Bathymetric data were obtained from the National Geophysical Data Center (NGDC, http://www.ngdc.noaa.gov) and GEBCO (http://www.gebco.net); free-air gravity anomaly (FAA) data were from Sandwell and Smith (2009); sediment thickness data were from the NGDC database (Divins, 2003); and the crustal age data were from Müller (2008).

(2) *Thermal Correction.* The gravity effects due to age-dependent cooling of the oceanic lithosphere were calculated from a 1-D plate cooling model, assuming the top and bottom temperatures of a 100-km-thick mantle layer with T_S=0°C and T_m=1,350°C, respectively (Turcotte and Schubert, 2002). The calculated thermal structure was then converted into a 3-D mantle density grid, in which the density anomaly $\Delta\rho = -\alpha\rho_0(T - T_0)$, where T is mantle temperature, T_0 = 1,350°C and ρ_0 = 3.3*10^3 kg/m^3 are reference temperature and density, respectively, and α = 3*10^{-5} °C^{-1} is the volumetric coefficient of thermal expansion.

(3) *Residual Mantle Bouguer Anomaly.* Assuming a reference crustal thickness of 6 km, the gravitational effects of the water/crust and crust/mantle density interfaces were removed from the FAA using the Parker spectrum method (Parker, 1973) to obtain the mantle Bouguer anomaly (MBA). The gravitational effects of lithospheric cooling, as calculated in the above Step 2, were then removed from the MBA to obtain residual mantle Bouguer anomaly (RMBA).

(4) *Crustal Thickness.* The crustal thickness was calculated from downward continuation of the RMBA signal to a reference depth using the methods of Parker (1973) and Kuo and Forsyth (1988). The best-fitting parameters of mantle and crustal densities used in the calculations were obtained from calibration of the gravity-derived models with constraints from available seismic refraction profiles.